INTERNATIONAL JOURNAL FOR NUMERICAL METHODS IN FLUIDS
Int. J. Numer. Meth. Fluids 2009; **61**:1063–1097
Published online 8 January 2009 in Wiley InterScience (www.interscience.wiley.com). DOI: 10.1002/fld.1983

A visual incompressible magneto-hydrodynamics solver with radiation, mass, and heat transfer

Necdet Aslan*,†

Physics Department, Yeditepe University, Kayışdağı, 34755 İstanbul, Turkey

SUMMARY

A visual two-dimensional (2D) nonlinear magneto-hydrodynamics (MHD) code that is able to solve steady state or transient charged or neutral convection problems under the radiation, mass, and heat transfer effects is presented. The flows considered are incompressible and the divergence conditions on the velocity and magnetic fields are handled by similar relaxation schemes in the form of pseudo-iterations between the real time levels. The numerical method utilizes a matrix distribution scheme that runs on structured or unstructured triangular meshes. The time-dependent algorithm developed here utilizes a semi-implicit dual time stepping technique with multistage Runge-Kutta (RK) algorithm. It is possible for the user to choose different normalizations (natural, forced, Boussinesq, Prandtl, double-diffusive and radiation convection) automatically. The code is visual and runs interactively with the user. The graphics algorithms work multithreaded and allow the user to follow certain flow features (color graphs, vector graphs, one-dimensional profiles) during runs, see (*Comput. Fluids* 2007; **36**:961–973) for details. With the code presented here nonlinear steady or time-dependent evolution of heated and stratified neutral and charged liquids, convection of mixture of neutral and charged gases, double-diffusive and salinity natural convection flows with internal heat generation/absorption and radiative heat transfer flows can be investigated. In addition, the numerical method (combining concentration, radiation, heat transfer, and MHD effects) takes the advantage of local time stepping and employs simplified residual jacobian matrix to increase pseudo-convergence rate. This code is currently being improved to simulate three-dimensional problems with parallel processing. Copyright © 2009 John Wiley & Sons, Ltd.

Received 6 March 2008; Revised 13 August 2008; Accepted 8 November 2008

KEY WORDS: magneto-hydrodynamics; incompressible; heat transfer; mass transfer; plasma; visual code; flows

*Correspondence to: Necdet Aslan, Physics Department, Yeditepe University, Kayışdağı, 34755 İstanbul, Turkey.
†E-mail: naslan@yeditepe.edu.tr

Contract/grant sponsor: NATO-CSP, COST-EU, TUBITAK-TR

1. RADIATION MAGNETO-HYDRODYNAMIC EQUATIONS

The fluid flows considered in this work are characterized by two-dimensional (2D) incompressible Navier–Stokes plus Maxwell's equations (i.e. MHD: magneto-hydrodynamic equations). The MHD system is coupled to the temperature and concentration effects through gravitational force by means of Bousinessq approximation and the fluid may experience radiative heat transfer. It is assumed that the solution medium is optically thick so that the change in the radiation density is negligible over radiation mean free path. In this 'diffusion approximation', there exists a local equilibrium between the radiation field and the charged fluid [1]. The starting point for the derivations of governing equations is non-relativistic equations of radiation MHD (i.e. conservation of mass, momentum, magnetic flux, and total energy) given by

$$\frac{\partial \mathbf{U}}{\partial t}+\nabla\cdot\widetilde{\mathbf{F}}_{\ell}=\frac{\partial \mathbf{U}}{\partial t}+\frac{\partial \mathbf{F}}{\partial x}+\frac{\partial \mathbf{G}}{\partial y}=\mathbf{S} \tag{1}$$

where the conservative state vector, $\mathbf{U}$, and the flux vectors $\mathbf{F}$ and $\mathbf{G}$ containing radiation effects are given by

$$\mathbf{U}=[\rho,\rho u+M_x^{\mathrm{r}},\rho v+M_y^{\mathrm{r}},B_x,B_y,E^{\mathrm{T}}+U^{\mathrm{r}}]^{\mathrm{T}} \tag{2}$$

$$\mathbf{F}=\begin{bmatrix}\rho u\\ \rho u^2+P^*-\dfrac{B_x^2}{\mu_0}-\tau_{xx}+T_{xx}^{\mathrm{r}}\\ \rho uv-\tau_{xy}+T_{xy}^{\mathrm{r}}\\ 0\\ uB_y-B_xv\\ \rho H^*u-\dfrac{B_x}{\mu_0}\mathbf{B}\cdot\mathbf{V}-Q_x+S_x^{\mathrm{r}}\end{bmatrix},\quad \mathbf{G}=\begin{bmatrix}\rho v\\ \rho uv-\tau_{yx}+T_{yx}^{\mathrm{r}}\\ \rho v^2+P^*-\dfrac{B_y^2}{\mu_0}-\tau_{yy}+T_{yy}^{\mathrm{r}}\\ uB_y-B_xv\\ 0\\ \rho H^*v-\dfrac{B_y}{\mu_0}\mathbf{B}\cdot\mathbf{V}-Q_y+S_y^{\mathrm{r}}\end{bmatrix} \tag{3}$$

where ρ is the density, $\mathbf{V}=(u,v)$ is the velocity, $\mathbf{B}=(B_x,B_y)$ is the magnetic field, $P^*=P+B^2/2\mu_0$ is the total pressure, $H^*=(E^{\mathrm{T}}+P^*)/\rho$ is the total enthalpy, $\mathbf{M}^{\mathrm{r}}=(M_x^{\mathrm{r}},M_y^{\mathrm{r}})$ is the radiation momentum density, U^{r} is the radiation energy density, and E^{T} is the non-radiative total energy density defined by

$$E^{\mathrm{T}}=\frac{P}{\gamma-1}+\frac{1}{2}\rho(u^2+v^2)+\frac{B^2}{2\mu_0} \tag{4}$$

where P is the scalar pressure and γ is the ratio of specific heats, μ_0 is magnetic permeability. In addition, $Q_{x,y}=(\overline{\overline{\tau}}\cdot\mathbf{V})_{x,y}-kT_{x,y}$ are heat fluxes (with k, the thermal conductivity), $\tau_{ij}=\mu(\partial V_j/\partial x_i+\partial V_i/\partial x_j)-\frac{2}{3}(\nabla\cdot\mathbf{V})\delta_{ij}$ is the viscosity tensor (with μ, the viscosity), $S_{x,y}^{\mathrm{r}}$ is the radiation flux and T^{r} is the radiation momentum flux. The source vector on the right side of Equation (1) is given by

$$\mathbf{S}=[0,F_x^m,F_y^m,F_x^B,F_y^B,\rho\mathbf{V}\cdot\mathbf{F}+q]^{\mathrm{T}} \tag{5}$$

DOI: 10.1002/fld

where $\mathbf{F}^m$ and $\mathbf{F}^B$ represent sources for momentum and magnetic fields, respectively, and q is the heat source. As an example, the gravitational effects in the y direction give rise to $F_x^m = 0$ and $F_y^m = -\rho g$ where g is the acceleration due to gravity. The radiation energy, radiation energy flux, and momentum flux tensor are given, respectively, by

$$U^{\mathrm{r}} = \int\int h\nu \mathbf{f}_{\mathrm{r}}\, \mathrm{d}\boldsymbol{\Omega}\, \mathrm{d}\nu, \quad \mathbf{S}^{\mathbf{r}} = \int\int h\nu \boldsymbol{\Omega} f_{\mathrm{r}}\, \mathrm{d}\boldsymbol{\Omega}\, \mathrm{d}\nu, \quad \overline{\overline{T^{\mathrm{r}}}} = \int\int h\nu \boldsymbol{\Omega}\boldsymbol{\Omega} f_{\mathrm{r}}\, \mathrm{d}\boldsymbol{\Omega}\, \mathrm{d}\nu \tag{6}$$

where ν is the radiation photon frequency, h is Planck constant, $\boldsymbol{\Omega}$ is the solid angle through which the photon propagates, and $f_{\mathrm{r}}(\nu, \boldsymbol{\Omega}, \mathbf{r}, t)$ is the photon distribution function.

The conservation equations given by Equation (1) to be supplemented by the divergence conditions on magnetic field:

$$\nabla \cdot \mathbf{B} = 0 \tag{7}$$

which expresses the fact that magnetic monopoles do not exist. Initially, Equation (7) is satisfied but if no action is taken, the numerical errors in divergence condition cumulates and causes the production of unphysical magnetic monopoles and magnetic sinks. Successful methods to cure this problem have been introduced in [3–5] and the references therein. Pseudo-iterations and artificial relaxation technique is used in this work.

2. CONCENTRATION EFFECTS

It is allowed in this work that the fluid may include species with different chemical properties. In that case, mass diffusion occurs whenever there is a concentration gradient in one of the species. The concentration effects can be derived from the following mass conservation equations for each species (here a total of 2 species is considered):

$$\frac{\partial \rho_i}{\partial t} + \nabla \cdot (\rho_i \mathbf{V}_i) = \frac{\delta m_i}{\delta t} \tag{8}$$

where the term on the right side represents the volumetric rate of creation of species i due to chemical reaction (which was considered negligible in this work). By summing these equations over species, one recovers the mass conservation law given by the first of Equation (1) with the exception that now, the fluid flows with the bulk fluid velocity: $\mathbf{V} = (\rho_1 \mathbf{V}_1 + \rho_2 \mathbf{V}_2)/\rho$ where $\rho = \rho_1 + \rho_2$ is the total density.

To distinguish the relative concentrations of different chemical properties of the flow, the diffusion mass fluxes (i.e. $\mathbf{J}_i = \rho_i(\mathbf{V}_i - \mathbf{V})$) can be used in Equation (8) to get

$$\frac{\partial \rho_i}{\partial t} + \nabla \cdot (\rho_i \mathbf{V}) = -\nabla \cdot \mathbf{J}_i \tag{9}$$

When the mass flux of species is due to the mass concentration gradient, one can use Fick's law given by $\mathbf{J}_i = -D\nabla\rho_i$ for the mass flux where D is the mass diffusivity of species 2 (salt, ethanol, etc.). Thus, for the incompressible mixture flows (i.e. $\nabla \cdot \mathbf{V} = 0$) the following concentration equation that governs the motion of one of the chemical species (i.e. here $C = \rho_2/\rho$) can be obtained

$$\frac{\partial C}{\partial t} + \mathbf{V} \cdot \nabla C = D\nabla^2 C \tag{10}$$

DOI: 10.1002/fld

When this equation is solved along with regular Navier–Stokes equations, concentration effects in the fluid are obtained. Notice that in this case, the effect of concentration appears as the gravitational source term through Boussinesq approximation (BA).

3. RADIATIVE EFFECTS

In the systems involving high temperatures (i.e. hypersonic flows, plasma physics, liquid metal environments, and furnace engineering) radiation effects should be considered along with the internal heat generation rate, i.e. q in Equation (5).

The radiation terms given in Equations (1), (3) are dependent upon the coordinate system in which they are measured and it is more convenient to transform them to the (primed) reference frame of fluid particles as follows:

$$\overline{\overline{T^{\mathrm{r}}}}'=\overline{\overline{T^{\mathrm{r}}}},\quad U^{\mathrm{r}\prime}=U^{\mathrm{r}},\quad \mathbf{S}^{\mathrm{r}\prime}=\mathbf{S}^{\mathrm{r}}-\mathbf{V}U^{\mathrm{r}\prime}-\mathbf{V}\cdot\overline{\overline{T^{\mathrm{r}}}} \tag{11}$$

When the radiation field is isotropic and radiation intensity weakly depends on the propagation angle, the radiating fluid is said to be radiatively opaque. In this thermal equilibrium case, the radiation energy and radiation flux vector can be written as $U_{\mathrm{r}}=4\sigma^{*}T^{4}/c$ and $S^{\mathrm{r}}=(c/3k^{*})\nabla U_{\mathrm{r}}$ where σ^{*} is the Stefan–Boltzmann constant, k^{*} is the radiation absorption constant, and c is the speed of light. Thus, the effect of radiation on the fluid momentum is now only through the radiation pressure, $P_{\mathrm{r}}U_{\mathrm{r}}/3$, which is the isotropic limit of $\overline{\overline{T^{\mathrm{r}}}}$. In that case, considering the transformations given in Equation (11), the equation of energy conservation turns into

$$\frac{\partial}{\partial t}(E^{\mathrm{T}}+U^{\mathrm{r}})+\nabla\cdot\left[(E^{\mathrm{T}}+U^{\mathrm{r}}+P+P_{\mathrm{r}})\mathbf{V}+k\nabla T-\frac{c}{3k^{*}}\nabla U_{\mathrm{r}}\right]=0 \tag{12}$$

Using the Rosseland approximation, further approximation is possible when the fluid is assumed to be absorbing and emitting radiation but not scattering it (see [4] for details). In this case, the effects of radiation pressure on fluid momentum are neglected resulting in the original momentum equation without radiation terms. In addition, U_{r} can also be neglected in comparison with the total energy. In that case, radiation flux term turns into the only term that survives in the energy equation. Thus, by using the thermodynamic identity: $dU=C_{p}dT$, Equation (12) can be converted into the following heat equation:

$$\rho C_{p}\left(\frac{\partial T}{\partial t}+\mathbf{V}\cdot\nabla T\right)=k\nabla^{2}T+\eta\mathbf{J}\cdot\mathbf{J}+q-\psi_{\mathrm{rad}} \tag{13}$$

where $\mathbf{J}$ is current density, η is resistivity and

$$\psi_{\mathrm{rad}}=\frac{4\sigma^{*}}{3k^{*}}\nabla^{2}(T^{4}) \tag{14}$$

is called the radiative heat flux source. In this work, different radiative approximations were considered. In optically thick limit, the fluid cannot absorb its own emitted radiation. In this non-gray fluid near equilibrium the radiative heat source can be taken as: $\psi_{\mathrm{rad}}=\mathrm{const}(T-T_{\infty})$ as shown by Cogly *et al.* [6]. When the fluid is gray it absorbs its radiation but does not scatter it.

DOI: 10.1002/fld

In that case the Rosseland approximation can be used and the radiative source can be linearized as: $T^4 \approx 4T_\infty^3 T - 3T_\infty^4$ as done in [4]. In this case, radiative heat source turns into

$$\psi_{\text{rad}} \approx \frac{4\sigma^*}{3k^*}\left[(1+rT)^3(\nabla^2 T)+3r(1+rT)^2\left(\left(\frac{\partial T}{\partial x}\right)^2+\left(\frac{\partial T}{\partial y}\right)^2\right)\right] \tag{15}$$

where $r = \Delta T / T_\infty$ is called the radiation source coefficient. The Rosseland approximation can also be used for optically thin fluid in which temperature gradients are so small that radiation source coefficient is negligible. In that case, $r \to 0$ and Equation (15) reduces to

$$\psi_{\text{rad}} \approx \frac{4\sigma^*}{3k^*}\left(\frac{\partial^2 T}{\partial y^2}\right) \tag{16}$$

when diffusion effects are negligible in the x direction.

These are the simplest approximations to include the radiative effects into the energy equation for incompressible flows. Full radiation MHD equations including the transport equations for the radiation are being developed by the author.

4. BOUSSINESQ APPROXIMATION

When gravitational forces are comparable to inertial and viscous forces for the low speed (incompressible) flows satisfying $\nabla \cdot \mathbf{V} = 0$, the temperature, concentration, and pressure effects (the latter much smaller than others) on the density should be included. To account for these effects, it is assumed that the density varies linearly with temperature and concentration according to the following BA:

$$\rho = \rho_0[1-\beta_T(T-T_0)+\beta_C(C-C_0)] \tag{17}$$

where ρ_0 is reference density, $\beta_T = -(1/\rho_0)\partial\rho/\partial T|_C$ and $\beta_C = (1/\rho_0)\partial\rho/\partial C|_T$ are the expansion coefficients due to temperature and concentration, respectively. When gravitational effects are included and Equation (17) is used, the vertical momentum source, F_y^m in Equation (5), can be written as

$$F_y^m = -\rho g = -\rho_0 g + \rho_0 g(\beta_T \Delta T + \beta_C \Delta C) \tag{18}$$

Note that the first term on the right-hand side of this equation will be combined with the pressure gradient terms in momentum equation as will be shown later.

Since BA approximation is a simple approximation for the mass conservation (or continuity) equation, its validity should be checked. Writing Equation (17) as

$$\Delta\rho = \beta_T \Delta T + \beta_C \Delta C$$

and differentiating it with respect to time one gets:

$$\frac{\partial \rho}{\partial t} = -\beta_T \frac{\partial T}{\partial t} + \beta_C \frac{\partial C}{\partial t} \tag{19}$$

DOI: 10.1002/fld

inserting $\partial C/\partial t$ and $\partial T/\partial t$ from Equations (10), (13) one gets:

$$\frac{\partial \rho}{\partial t}+\mathbf{V}\cdot(\beta_C \nabla C-\beta_T \nabla T)=\frac{\partial \rho}{\partial t}+\mathbf{V}\cdot\nabla\rho=\varepsilon$$

where

$$\varepsilon=\frac{\beta_T}{C_p}\left[k\nabla^2 T+q+\frac{4\sigma}{3k^*}\nabla^2(T^4)\right]+D\rho_0\beta_C\nabla^2 C \tag{20}$$

happens to be the error term of BA. This term is very small since the factor multiplying the first bracket of Equation (20) is negligible. For example, for water at atmospheric pressures $\beta_T \approx 3\times 10^{-4}\,\mathrm{K}^{-1}$ and $C_p \approx 4\times 10^3\,\mathrm{J/kg\,K}$ for temperatures less than 100°C this factor becomes nearly $0.75\times 10^{-7}\,\mathrm{kg/J}$. Similarly, for mixtures, $D\beta_C$ is also a very small number. Thus, when internal heat production is not very strong and temperature and concentration gradients are not very large, this error is usually very small so that the BA produces rather accurate solutions for buoyant natural mixture flows for a wide range of parameters. Thus, BA can be used to get an accurate coupling of temperature and concentration effects to the momentum equations through the gravitational source. Note that this coupling provides a good approximation for the equation of state, $\rho=\rho(T,C)$ when the departures from the reference density, $\rho_0=\rho(T_0,C_0)$ is small enough.

5. DIVERGENCE CONDITIONS AND PSEUDO-ITERATIONS

Because of the divergence conditions in velocity and magnetic fields, the incompressible system given by Equation (24) is numerically very difficult to solve. Although there exists different techniques to handle this problem, the easiest and most robust technique is to add pseudo-time derivatives of all variables and modify divergence conditions as

$$\frac{1}{\beta^2}\frac{\partial P'}{\partial \tau}+\nabla\cdot\mathbf{V}=0,\quad \frac{1}{\delta^2}\frac{\partial \Psi}{\partial \tau}+\nabla\cdot\mathbf{B}=0 \tag{21}$$

where τ is the pseudo-time, β^2 and δ^2 are artificial compressibility and magnetic relaxation factors and Ψ is called artificial magnetic flux function whose gradient is inserted in Faraday's law as a Lagrange multiplier to enforce divergence condition on magnetic field:

$$\frac{\partial \mathbf{B}}{\partial t}+\nabla\times(\mathbf{V}\times\mathbf{B})+\nabla\Psi=\frac{\eta}{\mu_0}\nabla^2\mathbf{B} \tag{22}$$

Note that Ψ also satisfies $\nabla^2\Psi=(\eta/\mu_0)\nabla\cdot(\nabla^2\mathbf{B})$ but it is not necessary to solve this equation if $\Psi=0$ is used as both initial and boundary conditions. In that case, Ψ becomes significant only at mesh points where divergence condition is violated and it acts as a Lagrange multiplier to dissipate this problem. Note that similar ideas have been used in [2, 7, 8]. The addition of pseudo-time derivatives and modifying divergence conditions are indeed some kind of preconditioning technique whose details for Navier–Stokes equations can be found in [9, 10].

DOI: 10.1002/fld

In this work, conservation laws given by Equation (1) are written in primitive form since incompressible flows with no shocks and discontinuities are considered in this work. In two dimensions Equation (1) becomes:

$$\frac{\partial U}{\partial W}\frac{\partial \mathbf{W}}{\partial t}+\frac{\partial F}{\partial U}\frac{\partial U}{\partial W}\frac{\partial \mathbf{W}}{\partial x}+\frac{\partial G}{\partial U}\frac{\partial U}{\partial W}\frac{\partial \mathbf{W}}{\partial y}=\mathbf{S}(\mathbf{U}) \tag{23}$$

where $\mathbf{W}$ is the primitive state vector to be described soon and $U_W=\partial U/\partial W$ is the conservative-to-primitive jacobian matrix. Pre-multiplying Equation (1) by the inverse of U_W, one gets

$$\frac{\partial \mathbf{W}}{\partial t}+A\frac{\partial \mathbf{W}}{\partial x}+B\frac{\partial \mathbf{W}}{\partial y}=\mathbf{S}(\mathbf{W}) \tag{24}$$

where $A=U_W^{-1}F_U U_W$ and $B=U_W^{-1}G_U U_W$ are now called as primitive flux jacobian matrices and $\mathbf{S}(\mathbf{W})=U_W^{-1}\mathbf{S}(\mathbf{U})$ is the primitive source vector. As stated earlier, these equations are modified by inserting pseudo-time derivatives as follows:

$$\frac{\partial \mathbf{W}}{\partial \tau}+I_\tau\frac{\partial \mathbf{W}}{\partial t}+A\frac{\partial \mathbf{W}}{\partial x}+B\frac{\partial \mathbf{W}}{\partial y}=\mathbf{S}(\mathbf{W}) \tag{25}$$

where $I_\tau=\text{diag}[0,1,1,1,1,1,1,0]$ is the diagonal matrix used to eliminate divergence conditions from real time advancements as it has been used in [11] for the numerical solutions of Navier–Stokes equations. The pseudo-time iterations are applied between each time level until convergence is established in pseudo-time (i.e. $\partial\mathbf{W}/\partial\tau\to 0$), so that Equation (25) reduces to Equation (24) provided that the divergence conditions are satisfied within a pre-specified tolerance. Note that as $\partial P', \Psi/\partial\tau\to 0$ then divergence conditions in Equation (21) are satisfied regardless of the values of β^2 and δ^2, which are usually taken within the interval [12, 13].

6. DIMENSIONLESS EQUATIONS

The incompressible MHD equations obtained with this procedure produce useful solutions when they are cast into a dimensionless form since the flow properties depend upon the physical parameters, such as viscosity and resistivity. In this work, the space $\mathbf{r}=(\mathbf{x},\mathbf{y})$, time, velocity, temperature, concentration, pressure, and electric and magnetic fields as well as Ψ were made dimensionless using

$$\begin{gathered} x', y'=x, y/L, \quad t'=t/t_0, \quad \mathbf{V}'=\mathbf{V}/V_0 \\ \theta=\frac{T-T_1}{\Delta T}, \quad C'=\frac{C-C_1}{\Delta C}, \quad P'=\frac{P+\rho_0 g y}{P_0}, \quad \mathbf{E}'=\frac{\mathbf{E}}{E_0}, \quad \mathbf{B}'=\frac{\mathbf{B}}{B_0}, \quad \Psi'=\frac{\Psi}{\Psi_0} \end{gathered} \tag{26}$$

where $\Delta T=T_2-T_1$, $\Delta C=C_2-C_1$ while $T_{1,2}$ and $C_{1,2}$ can be selected to specify wall or free-stream conditions as well as a specific normalization point. Note that by modifying pressure as $P^*=P+\rho_0 g y$, one has $\partial P/\partial x=\partial P^*/\partial x$ and $\partial P/\partial y=\partial P^*/\partial y-\rho_0 g$ so that the first term in Equation (18) can be absorbed in pressure.

The form of velocity normalization factor, V_0 specifies the type of normalizations. For forced or mixed convection (FC)

$$V_0=L/t_0 \tag{27}$$

DOI: 10.1002/fld

is taken, for natural convection (NC) $V_0=\kappa/L$ is chosen, for Boussinesq fluid convection (BC) $V_0=\nu/L$ is taken, for Prandtl fluid convection (PC) $V_0=\kappa\sqrt{Ra}/L$ and for radiation and mass convection $V_0=\nu/L$ are used. The dimensionless parameters used in this work are defined as

$$Re=\frac{LV_0}{\nu},\quad Pr=\frac{\nu}{k},\quad Ra_{T,C}=\frac{g\beta_{T,C}L^3\Delta(T,C)}{\kappa\nu},\quad Ra^{\mathrm{i}}=\frac{g\beta_T L^5 q'''}{\nu k\kappa},\quad Le=\frac{D}{\nu} \tag{28a}$$

$$Fr=\frac{4\sigma^* T_0^3}{kk^*},\quad N=\frac{\sigma B_0^2 L_0}{\rho_0 V_0},\quad Ec=\frac{V_0^2}{C_p\Delta T},\quad Sc=\frac{\nu}{D},\quad Re_{\mathrm{m}}=\mu_0\sigma V_0 L_0 \tag{28b}$$

where Re is Reynolds number, Pr is the Prandtl number, Ra is the Rayleigh number, Ra^{i} is the internal Rayleigh number, Fr is the Froudes number, N is magnetic interaction parameter, Ec is the Eckert number, Sc is Schmidt number and Re_{m} is magnetic Reynolds number. In addition, where $\nu=\mu/\rho_0$ is the kinematic viscosity, k is the thermal conductivity, $\kappa=k/\rho_0 C_p$ is the thermal diffusivity, $\sigma=1/\eta$ is the electrical conductivity, C_p is the ratio of specific heats, and k^* is the mean radiation absorption coefficient. With the normalization used here, the following relationship among the dimensional parameters are found: $P_0=\rho_0 V_0^2=B_0^2/\mu_0=E_0/V_0$.

The dimensionless form of incompressible MHD equations including radiation, concentration, and heat transfer effects can be explicitly written as:

$$\frac{1}{\beta^2}\frac{\partial P'}{\partial\tau}+\frac{\partial u}{\partial x}+\frac{\partial v}{\partial y}=0 \tag{29}$$

$$\frac{\partial u}{\partial\tau}+\frac{\partial u}{\partial t}+u\frac{\partial u}{\partial x}+v\frac{\partial u}{\partial y}+\frac{\partial P'}{\partial x}=N_V^*\nabla^2 u+N_B^* F_x+\frac{N}{Re_{\mathrm{m}}}(\mathbf{J}\times\mathbf{B})_x \tag{30}$$

$$\frac{\partial v}{\partial\tau}+\frac{\partial v}{\partial t}+u\frac{\partial v}{\partial x}+v\frac{\partial v}{\partial y}+\frac{\partial P'}{\partial y}=N_V^*\nabla^2 v+N_B^* F_y+\frac{N}{Re_{\mathrm{m}}}(\mathbf{J}\times\mathbf{B})_y \tag{31}$$

$$\frac{\partial\theta}{\partial\tau}+\frac{\partial\theta}{\partial t}+u\frac{\partial\theta}{\partial x}+v\frac{\partial\theta}{\partial y}=N_\theta^*\nabla^2\theta+N_\psi^*\Psi_{\mathrm{rad}}+N_{\mathrm{heat}}^*+NEc\mathbf{J}\cdot\mathbf{J} \tag{32}$$

$$\frac{\partial C}{\partial\tau}+\frac{\partial C}{\partial t}+u\frac{\partial C}{\partial x}+v\frac{\partial C}{\partial y}=N_C^*\nabla^2 C \tag{33}$$

$$\frac{\partial B_x}{\partial\tau}+\frac{\partial B_x}{\partial t}+u\frac{\partial B_x}{\partial x}+v\frac{\partial B_x}{\partial y}-B_y\frac{\partial u}{\partial y}-B_x\frac{\partial u}{\partial x}=\frac{1}{Re_{\mathrm{m}}}\nabla^2 B_x \tag{34}$$

$$\frac{\partial B_y}{\partial\tau}+\frac{\partial B_y}{\partial t}+u\frac{\partial B_y}{\partial x}+v\frac{\partial B_y}{\partial y}-B_x\frac{\partial v}{\partial x}-B_y\frac{\partial v}{\partial y}=\frac{1}{Re_{\mathrm{m}}}\nabla^2 B_y \tag{35}$$

$$\frac{1}{\delta^2}\frac{\partial\Psi}{\partial\tau}+\frac{\partial B_x}{\partial x}+\frac{\partial B_y}{\partial y}=0 \tag{36}$$

Note that the current density in Equations (30)–(32) can be taken either from Ohm's law given by:

$$\mathbf{J}=(\mathbf{E}^{\mathrm{ext}}+\mathbf{V}\times\mathbf{B})/\eta=\nabla\times\mathbf{B}/\mu_0 \tag{37}$$

DOI: 10.1002/fld

Table I. Normalization types and dimensional parameters.

	N_V^*	N_B^*	N_θ^*	N_{heat}^*	N_C^*
FC	$1/Re$	Gr/Re^2	$1/RePr$	$Ra_i/Pr\,Ra\,Re$	$Le/PrRe$
NC	Pr	$GrPr^2$	1	Ra_i/Ra	Le
BC	1	Ra/Pr	$1/Pr$	$Ra_i/PrRa$	Le/Pr
PC	$Pr/\sqrt{Ra}$	Pr	$1/\sqrt{Ra}$	$Ra_i/Ra^{3/2}$	$Le/\sqrt{Ra}$
RC	1	Gr	$1/Pr$	$Ra_i/PrRa$	$1/Sc$
DD	Pr	$Ra_T\,Pr$	1	0	$1/Le$

FC: $V_0 = L/t_0$, NC: $V_0 = \kappa/L$, BC: $V_0 = \nu/L$, PC: $V_0 = \kappa\sqrt{Ra}/L$, DD: $V_0 = L/\kappa$.

or from Ampere's law:

$$\mathbf{J} = \frac{1}{\mu_0}\nabla \times \mathbf{B} \tag{38}$$

In addition, $N_V^*, N_B^*, N_\theta^*, N_{\text{heat}}^*, N_C^*, N_\psi^*, N_{\text{heat}}$ denote the normalization parameters whose forms depend on different normalizations listed in Table I. Note that, if the first term of Equation (18) is combined with $\partial P/\partial y$ in the y-momentum equation, the rest of the term in this equation gives rise to the following source for v-velocity:

$$S_2 = N_B^*(\theta + NC') \tag{39}$$

After making the equations dimensionless, the primitive state used in Equations (23)–(25) is defined as:

$$\mathbf{W} = [P', u, v, \theta, C, B_x, B_y, \Psi]^{\mathrm{T}} \tag{40}$$

The coefficients of $\partial\mathbf{W}/\partial x$ as presented in Equation (25) give rise to the following jacobian matrix, $A(\beta^2, \delta^2)$:

$$A = \begin{bmatrix} 0 & \beta^2 & 0 & 0 & 0 & 0 & 0 & 0 \\ 1 & u & 0 & 0 & 0 & 0 & \dfrac{NB_y}{Re_{\text{m}}} & 0 \\ 0 & 0 & u & 0 & 0 & 0 & -\dfrac{NB_x}{Re_{\text{m}}} & 0 \\ 0 & 0 & 0 & u & 0 & 0 & 0 & \dfrac{NEB_x}{Re_{\text{m}}} \\ 0 & 0 & 0 & 0 & u & 0 & 0 & 0 \\ 0 & -B_x & 0 & 0 & 0 & u & 0 & 1 \\ 0 & 0 & -B_x & 0 & 0 & 0 & u & 0 \\ 0 & 0 & 0 & 0 & 0 & \delta^2 & 0 & 0 \end{bmatrix} \tag{41}$$

DOI: 10.1002/fld

and the viscous and source terms give rise to the following source vector:

$$\mathbf{S}=\begin{bmatrix} 0 \\ N_V^*\nabla^2 u+\dfrac{N}{Re_{\mathrm{m}}}(\mathbf{J}\times\mathbf{B})_x \\ N_V^*\nabla^2 v+N_B^*(\theta+NC)+\dfrac{N}{Re_{\mathrm{m}}}(\mathbf{J}\times\mathbf{B})_y \\ N_\theta^*\nabla^2\theta+N_\Psi^*\Psi_{\mathrm{rad}}+N_{\mathrm{heat}}+NEc\mathbf{J}\cdot\mathbf{J} \\ N_C^*\nabla^2 C \\ \dfrac{1}{Re_{\mathrm{m}}}\nabla^2 B_x \\ \dfrac{1}{Re_{\mathrm{m}}}\nabla^2 B_y \\ 0 \end{bmatrix} \tag{42}$$

where $\mathbf{J}\cdot\mathbf{J}=\mathbf{J}^2$ is the heat source due to electric currents. Note that the jacobian matrix, B, can be obtained by interchanging $\frac{2.}{3.}$ and $\frac{6.}{7.}$ columns and rows of A. Note that using the RC normalization (given in Table I) for radiative heat transfer problems and taking $N_\Psi^*=1/N_{\mathrm{rad}}Pr$, the radiation source can be written as

$$\Psi_{\mathrm{rad}}=-\frac{4}{3N_{\mathrm{rad}}Pr}\left[(1+r\theta)^3(\nabla^2\theta)+3r(1+r\theta)^2\left(\left(\frac{\partial\theta}{\partial x}\right)^2+\left(\frac{\partial\theta}{\partial y}\right)^2\right)\right] \tag{43}$$

where $r=\Delta\theta/\theta_\infty$ is the radiation source coefficient and θ_∞ is the reference temperature. Note that this term introduces higher-order thermal gradients into the scheme in order to include very simple radiative effects.

7. SPATIAL DISCRETIZATION: MATRIX DISTRIBUTION

A matrix distribution (MD) scheme was used for the spatial discretization of the MHD equations given by Equation (24). In this scheme, $\mathbf{W}$ was assumed to change linearly within the triangles satisfying

$$\mathbf{W}(x,y,t)=\sum_k^M \mathbf{W}_k(t)N_k(x,y) \tag{44}$$

where M is the total number of neighbor nodes around node k of triangle T, $\mathbf{W}_k(t)$ is the value of $\mathbf{W}$ at node k and $N_k(x_\ell,y_\ell)=\delta_{k,\ell}$ is the linear shape function shown in Figure 1. Since the variables are located at the vertices (nodes) of triangular mesh, the median dual cell (veroni) area, Ω_k, around a typical node, k, is obtained by connecting the cell centers through the area boundary given by $\delta\Omega_k$, see Figure 1(b). In order to accomplish the spatial integration of MHD equations

DOI: 10.1002/fld

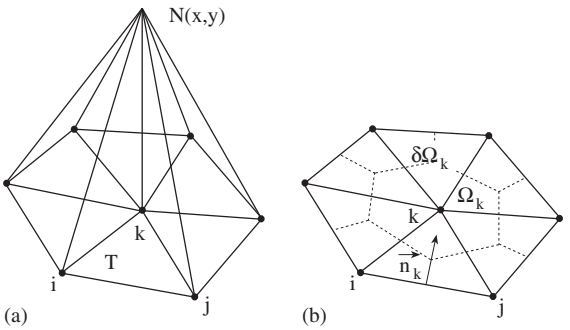

Figure 1. (a) The linear shape function above node k of triangle T and (b) inward normal, $\vec{n}_k$ across node k, median dual cell area, Ω_k and its boundary, $\delta\Omega_k$.

over such an area, Equation (25) is multiplied by a linear test function $w_\ell(x, y)$ that vanishes on $\delta\Omega_\ell$ and it is integrated over the area

$$\int\int_\Omega \left[\frac{\partial \mathbf{W}}{\partial \tau} + I_\tau \frac{\partial \mathbf{W}}{\partial t}\right] w_\ell \, \mathrm{d}\Omega + \int\int_\Omega \left[A\frac{\partial \mathbf{W}}{\partial x} + B\frac{\partial \mathbf{W}}{\partial y}\right] w_\ell \, \mathrm{d}\Omega = \int\int_\Omega [\mathbf{S}] w_\ell \, \mathrm{d}\Omega \tag{45}$$

Using Equation (44) the first integral in Equation (45) becomes

$$\int\int_\Omega w_\ell \sum_{k=1}^{M} N_k \left[\frac{\partial \mathbf{W}_k}{\partial \tau} + I_\tau \frac{\partial \mathbf{W}_k}{\partial t}\right] \mathrm{d}\Omega = \sum_{k=1}^{m} M_{\ell,k} \left[\frac{\partial \mathbf{W}_k}{\partial \tau} + I_\tau \frac{\partial \mathbf{W}_k}{\partial t}\right] \tag{46}$$

where $M_{\ell,k}$ is the element of the lumped mass matrix given by $M = \int\int_\Omega w_\ell N_k \, \mathrm{d}\Omega$. By taking $W_\ell = N_\ell$ one gets $M = \int\int_\Omega N_\ell N_k \, \mathrm{d}\Omega = \sum_{T\in\ell} \delta_{\ell,k}$ and writing the global system as the summation over triangles (i.e. $\sum_{k=1}^{M} \to \sum_{T\in\Omega_\ell} \sum_{k=1}^{3}$), Equation (46) becomes:

$$\sum_{T\in\Omega_\ell} \sum_{k=1}^{3} \frac{\Omega_T}{3} \delta_{\ell,k} \left[\frac{\partial \mathbf{W}_k}{\partial \tau} + I_\tau \frac{\partial \mathbf{W}_k}{\partial t}\right] = \Omega_\ell \left[\frac{\partial \mathbf{W}_\ell}{\partial \tau} + I_\tau \frac{\partial \mathbf{W}_\ell}{\partial t}\right] \tag{47}$$

where now Ω_ℓ is the median dual cell area around node ℓ. Inserting Equation (44) into the convective terms (second integral) in Equation (45) one gets

$$\int\int_\Omega N_\ell \left[A\frac{\partial \mathbf{W}}{\partial x} + B\frac{\partial \mathbf{W}}{\partial y}\right] \mathrm{d}\Omega = \int\int_\Omega N_\ell \sum_{k=1}^{M} \left[A\mathbf{W}_k \frac{\partial N_k}{\partial x} + B\mathbf{W}_k \frac{\partial N_k}{\partial y}\right] \mathrm{d}\Omega \tag{48}$$

Note that since $N(x, t)$ is linear over the triangle, its gradient is constant and given by: $\nabla N_k = \mathbf{n}_k / 2\Omega_T$ where $\mathbf{n}_k$ is the inward edge normal vector across the node k and scaled by its length, see Figure 1(b). Using Gauss' theorem and trapezoidal rule for integration, the right hand side of Equation (48) can be written as

$$= \oint_{\delta\Omega} N_\ell \sum_{k=1}^{M} \frac{1}{2} [A\mathbf{W}_k n_{k,x} + B\mathbf{W}_k n_{k,y}] \, \mathrm{d}\Omega = \sum_{T\in\Omega_\ell} \oint_{\delta\Omega_T} N_\ell \sum_{k=1}^{3} K_k \mathbf{W}_k \, \mathrm{d}\Omega_T \tag{49}$$

where

$$K_k = \tfrac{1}{2} [A(\overline{\mathbf{W}}_k) n_{k,x} + B(\overline{\mathbf{W}}_k) n_{k,y}] \tag{50}$$

DOI: 10.1002/fld

is called flux matrix which characterizes the MHD system, $A(\overline{\mathbf{W}})$, $B(\overline{\mathbf{W}})$ are mesh-averaged jacobian matrices and $\overline{\mathbf{W}}=(\mathbf{W}_1+\mathbf{W}_2+\mathbf{W}_3)/3$ is mesh-averaged state vector. The characteristic speeds of the MHD system are indeed the eigenvalues of this matrix:

$$\lambda=V_v, V_n, \frac{1}{2}\left[V_n\pm\sqrt{V_n^2+4\beta^2}\right], \frac{1}{2}\left[V_n\pm\sqrt{V_n^2+4\alpha^2}\right], V_n\pm\sqrt{\frac{N}{Re_{\mathrm{m}}}B_n^2} \tag{51}$$

where $V_n=un_x+vn_y$ and $B_n=B_xn_x+B_yn_y$ are normal speed and magnetic field, respectively, and β^2 and α^2 act as artificial sound speeds arising from the divergence conditions on velocity and divergence, respectively. In calculating the pseudo-time step as given in Equation (64), the maximum value of these eigenvalues over the mesh is used.

Defining the mesh-averaged distribution matrix, B_ℓ^{T} and total fluctuation vector, $\mathbf{\Phi}_T$ as

$$B_\ell^{\mathrm{T}}=\frac{1}{\Omega_T}\iint N_\ell\,\mathrm{d}\Omega, \quad \mathbf{\Phi}_T=\sum_{i=1}^{3}K_i\mathbf{W}_i \tag{52}$$

Equation (48) becomes

$$\iint_\Omega\left[A\frac{\partial\mathbf{W}}{\partial x}+B\frac{\partial\mathbf{W}}{\partial y}\right]N_\ell\,\mathrm{d}\Omega=\sum_{T\in\Omega_\ell}B_\ell^{\mathrm{T}}\mathbf{\Phi}_T \tag{53}$$

which shows that the total fluctuation vector in the triangle is distributed to the node ℓ of triangle T using the weight matrix, B_ℓ^{T}. In addition, it can be shown that the source term on the right-hand side of Equation (45) becomes $\Omega_\ell\mathbf{S}_\ell$. When all the terms are collected, Equation (45) finally turns into

$$\Omega_\ell\left[\frac{\mathbf{W}_\ell}{\partial\tau}+I_\tau\frac{\partial\mathbf{W}_\ell}{\partial t}\right]+\sum_{T\in\Omega_\ell}B_\ell\Phi_T+\mathbf{S}_\ell\Omega_\ell \tag{54}$$

The distribution matrix can be derived by a second-order Lax-Wendrof-type scheme using the following Taylor's expansion:

$$\mathbf{W}^{n+1}(x,y)=\mathbf{W}^n(x,y)+\Delta t\frac{\partial\mathbf{W}}{\partial t}^n+\frac{\Delta t^2}{2}\frac{\partial^2\mathbf{W}}{\partial t^2}^n+\frac{\Delta t^3}{6}\frac{\partial^3\mathbf{W}}{\partial t^3}^n+\cdots \tag{55}$$

where n is the time level and Δt is the time step. First, writing Equation (24) as

$$\frac{\partial\mathbf{W}}{\partial t}=-A_i\frac{\partial\mathbf{W}}{\partial x_i}+\mathbf{S}, \quad i=1,2 \tag{56}$$

where $x_{1,2}=x, y$ and $A_{1,2}=A, B$ and inserting it into the above Taylor expansion one gets:

$$\mathbf{W}^{n+1}(x,y)-\mathbf{W}^n(x,y)=\Delta t\left(-A_i\frac{\partial\mathbf{W}}{\partial x_i}+\mathbf{S}\right)^n+\frac{\Delta t^2}{2}\frac{\partial}{\partial t}\left(-A_i\frac{\partial\mathbf{W}}{\partial x_i}+\mathbf{S}\right)^n+\cdots \tag{57}$$

Neglecting higher-order terms and integrating this equation over Ω_ℓ around node ℓ one gets:

$$\iint_{\Omega_\ell}(\mathbf{W}_\ell^{n+1}-\mathbf{W}_\ell^n)\,\mathrm{d}\Omega=\Delta t\iint_{\Omega_\ell}\left[\left(-A_i\frac{\partial\mathbf{W}_\ell}{\partial x_i}+\mathbf{S}_\ell\right)^n+\frac{\Delta t}{2}\frac{\partial}{\partial t}\left(-A_i\frac{\partial\mathbf{W}_\ell}{\partial x_i}+\mathbf{S}_\ell\right)^n\right]\mathrm{d}\Omega \tag{58}$$

DOI: 10.1002/fld

After trivial derivations as carried out earlier, one can show that the left-hand side of Equation (58) evaluated at node k of triangle T turns into: $(\mathbf{W}_\ell^{n+1}-\mathbf{W}_\ell^n)\Omega_\ell$, the first integral on its right-hand side becomes: $\Delta t\boldsymbol{\Phi}_T/3$ and the last integral becomes: $(\Delta t^2/2)(K_\ell/\Omega_T)\boldsymbol{\Phi}_T$ and finally the body source turns into: $\Delta t\mathbf{S}(\overline{\mathbf{W}})/3$, noting that the time derivative of the source was neglected.

By combining all these results, Equation (58) can be written as

$$\begin{aligned}(\mathbf{W}_\ell^{n+1}-\mathbf{W}_\ell^n)\Omega_\ell &= \Delta t\frac{\boldsymbol{\Phi}_T}{3}+\frac{\Delta t^2}{2\Omega_T}K_\ell\boldsymbol{\Phi}_T+\frac{\Delta t}{3}\Omega_\ell\mathbf{S}\\ &= \Delta t\left(\frac{1}{3}I+\frac{\Delta t}{2\Omega_T}K_\ell\right)\boldsymbol{\Phi}_T(\tilde{\mathbf{W}})+\frac{\Delta t}{3}\Omega_\ell\mathbf{S}(\overline{\mathbf{W}})\end{aligned} \tag{59}$$

showing that the simplified Lax-Wendroff weight matrix is given by:

$$B_\ell=\frac{1}{3}I+\frac{\Delta t^*}{2\Omega_T}K_\ell \tag{60}$$

where $\Delta t^*=\mathrm{CFL}\,h_{\min}/\lambda_{\max}$, $\lambda_{\max}$ is the maximum modulus of the eigenvalues given in Equation (51) and $h_{\min}$ is the minimum side length of the mesh with CFL$\leqslant$0.5, the CFL number. It must be noted here that regular system Lax-Wendroff weight matrix that requires inversion is given as (see [14])

$$B_\ell=\frac{1}{3}I+\mathrm{CFL}K_\ell\left(\sum_{m=1}^{3}|K_m|\right)^{-1} \tag{61}$$

This matrix is not used in the code presented here since it includes many off-diagonal terms and slows down the code significantly since it must be calculated for each node in the mesh. It is noted that different forms of distribution matrices can be used as stated in References [14–16] but numerical experience shows that using different forms of distribution matrix does not change the solutions appreciably, especially when steady state solutions are seeked.

With a trivial algebra, one can show that the viscous source terms given in Equation (58) can be written as $(\nu/4\Omega_T)\sum_{j=1}^{3}\mathbf{n}_\ell\cdot\mathbf{n}_j\mathbf{W}_j$.

When all the results are put together, the explicit pseudo-iterations for the solution vector at node ℓ of triangle T becomes:

$$\mathbf{W}_\ell^{m+1}=\mathbf{W}_\ell^m+\Delta\tau\left[\mathrm{Res}(\mathbf{W}_\ell)-I_\tau\frac{\partial\mathbf{W}_\ell}{\partial t}\right] \tag{62}$$

where

$$\mathrm{Res}(\mathbf{W}_\ell)=-\frac{1}{\Omega_\ell}\sum_{T\in\Omega_\ell}\left[B_\ell^{\mathrm{T}}\boldsymbol{\Phi}_T+\frac{\nu}{4\Omega_T}\sum_{j=1}^{3}\mathbf{n}_\ell\cdot\mathbf{n}_j\mathbf{W}_j-\mathbf{S}(\overline{\mathbf{W}})\frac{\Omega_T}{3}\right] \tag{63}$$

is the residual vector to be assigned to the state vector located at node ℓ of triangle T. It is noted that in order to increase temporal accuracy, this pseudo-time integration was carried with the Runge-Kutta (RK) algorithm (this will be described later).

DOI: 10.1002/fld

8. TEMPORAL DISCRETIZATION

In the numerical solutions it is better to use implicit methods for time derivatives since they are numerically stable for any value of Δt, the time step. But since these methods are very complicated for unstructured triangular grids, the pseudo-time iterations in this work were carried out by explicit multistage RK algorithm with the pseudo-time step calculated from the maximum eigenvalue of matrix K given in Equation (50):

$$\Delta\tau = \frac{\mathrm{CFL}}{\lambda_{\max}/h_{\min}} \tag{64}$$

In the numerical solutions, the real time advancement is done in such a way that the new solutions at $t = t^{n+1}$ is obtained from the previous time level, $t^n = n\Delta t$ where n is the real time level. The real time derivative in Equation (62) at the new time level is approximated as

$$\frac{\partial \mathbf{W}}{\partial t}^{n+1} = \frac{1+\phi}{\Delta t}(\mathbf{W}^{n+1} - \mathbf{W}^n) - \frac{\phi}{\Delta t}(\mathbf{W}^n - \mathbf{W}^{n-1}) \tag{65}$$

where $\phi = 0$ gives explicit first order while $\phi = 0.5$ gives the second-order accuracy in time ($\phi = 0.5$ was used in this work). Since pseudo-iterations are carried between consecutive real time levels, another subscript m is introduced to denote the pseudo-iteration level. Thus, $\mathbf{W}^{n,m}$ and $\mathrm{Res}^{n,m} = \mathrm{Res}(\mathbf{W}^{n,m})$ denote the state and residual vectors mth pseudo-iteration at time level, t^n.

Since the real time advancement requires that the variables are evaluated at the new time level $n+1$, Equation (65) is written as

$$\frac{\partial \mathbf{W}}{\partial \tau}^{n+1,m+1} + I_\tau \left[\frac{1+\phi}{\Delta t}(\mathbf{W}^{n+1,m+1} - \mathbf{W}^n) - \frac{\phi}{\Delta t}(\mathbf{W}^n - \mathbf{W}^{n-1}) \right] \mathrm{Res}^{n+1,m+1} \tag{66}$$

where $m = 1, 2, \ldots, M$ is the pseudo-iteration level. Notice that since the starting point of pseudo-iterations is time level t^n, there is no way of changing $\mathbf{W}^n$ and $\mathbf{W}^{n-1}$ during pseudo-iterations. This is the reason why the states $\mathbf{W}^n$ and $\mathbf{W}^{n-1}$ are written with single superscript. The reason of pseudo-iterations is to drive the velocity (and magnetic field) divergence to zero so that physically accepted results are obtained. As the pseudo-iterations converge, the solutions at new time level are obtained (i.e. $\mathbf{W}^{n+1,M} \to \mathbf{W}^{n+1}$).

In order to introduce some implicitness into the scheme, the residual at new pseudo-iteration level is approximated as

$$\mathrm{Res}^{n,m+1} \approx \mathrm{Res}^{n,m} + J^{n,m}(\mathbf{W}^{n,m+1} - \mathbf{W}^{n,m}) \tag{67}$$

where $J = \partial \mathrm{Res}/\partial \mathbf{W}$ is the jacobian matrix of the residual with respect to the state vector. Since it is simpler, only diagonal terms of this matrix are retained as done in [17]. The net effect of this matrix is to increase the pseudo-time convergence rate as will be shown in the following section. In order to show how this residual jacobian is obtained consider simple hydrodynamics case with $W = [P, u, v]^{\mathrm{T}}$. After trivial but tedious algebra (probably using a symbolic computation package

DOI: 10.1002/fld

such as Maple) one can show that the diagonal elements of residual jacobian (at node i of triangle T) are given by the following vector:

$$\mathbf{J_i}=\begin{bmatrix} \dfrac{\sigma\beta^2}{4} \\ \dfrac{\sigma n_{xi}}{4}(V_nU+P_{nx})+\left(\dfrac{\sigma V_{ni}}{2}+\dfrac{1}{3}\right)\left(V_{ni}-\dfrac{v_i n_{y_i}}{2}\right) \\ \dfrac{\sigma n_{y_i}}{4}(V_nV+P_{ny})+\dfrac{1}{2}\left(\dfrac{\sigma V_{ni}}{2}+\dfrac{1}{3}\right)(V_{ni}+v_i n_{y_i}) \end{bmatrix} \tag{68}$$

where $\sigma=\Delta t/2\Omega_T$, $P_{nx,y}=P_i n_{x,y_i}+P_j n_{x,y_j}+P_k n_{x,y_k}$, $V_nU=V_{ni}u_i+V_{nj}u_j+V_{nk}u_k$, $V_nV=V_{ni}v_i+V_{nj}v_j+V_{nk}v_k$ and $V_{ni}=n_{xi}u_i+n_{y_i}v_i$ and $n_{xi,j}$ and $n_{y_{i,j}}$ are x and y components of the inward normal vector on the edge across the node i of triangle T. Note that the existence of this jacobian matrix allows us to use higher CFL numbers and provides different local pseudo-time steppings for the solution vector. This is the reason why the pseudo-convergence (and hence overall convergence) rate increases.

In that case, the resulting explicit algorithm for the pseudo-time advancement of $\mathbf{W}$ at the nodes of triangle T can be written as

$$\frac{\mathbf{W}^{n+1,m+1}-\mathbf{W}^{n+1,m}}{\Delta\tau}=\mathrm{Res}(\mathbf{W})^{n+1,m}+J^{n,m}(\mathbf{W}^{n+1,m+1}-\mathbf{W}^{n+1,m}) \\ -I_\tau\left[\frac{1+\phi}{\Delta t}(\mathbf{W}^{n+1,m+1}-\mathbf{W}^n)-\frac{\phi}{\Delta t}(\mathbf{W}^n-\mathbf{W}^{n-1})\right] \tag{69}$$

By adding and subtracting $\mathbf{W}^{n+1,m}$ to the second term in Equation (69) and transferring $\Delta\mathbf{W}$ to the left-hand side, one gets

$$\left[I-J^{n,m}\Delta\tau+I_\tau\frac{1+\phi}{\Delta t}\Delta\tau\right](\mathbf{W}^{n+1,m+1}-\mathbf{W}^{n+1,m})=\Delta\tau\left[\mathrm{Res}^{n+1,m}-I_\tau\frac{\partial\mathbf{W}}{\partial t}^{n+1,m}\right] \tag{70}$$

where in this case the real time derivative can be evaluated from

$$\frac{\partial\mathbf{W}}{\partial t}^{n+1,m}=\frac{1+\phi}{\Delta t}(\mathbf{W}^{n+1,m}-\mathbf{W}^n)-\frac{\phi}{\Delta t}(\mathbf{W}^n-\mathbf{W}^{n-1}) \tag{71}$$

By defining new modified residual that includes both the time derivative and flux terms as

$$\widetilde{\mathrm{Res}}^{n+1,m}=\mathrm{Res}^{n+1,m}-I_\tau\frac{\partial\mathbf{W}}{\partial t}^{n+1,m} \tag{72}$$

the following semi-implicit algorithm is obtained for pseudo-iterations

$$\mathbf{W}^{n+1,m+1}=\mathbf{W}^{n+1,m}+\Delta\tau[I_\tau^*]^{-1}\widetilde{\mathrm{Res}}^{n+1,m} \tag{73}$$

DOI: 10.1002/fld

where $I_\tau^* = [I - J^{n,m}\Delta\tau + I_\tau((1+\phi)/\Delta t)\Delta\tau]$. Since the accuracy of the explicit methods is only of first order, multistage RK algorithm is used for pseudo-integration to increase temporal accuracy:

$$\begin{aligned} \mathbf{W}_0 &= \mathbf{W}^m \\ \mathbf{W}_{k+1}^{n,m} &= \mathbf{W}_0^{n,m}[I_\tau^*]^{-1}\alpha_k\Delta\tau[\widetilde{\mathrm{Res}}^{n,m}]_k \\ &\vdots \\ \mathbf{W}^{m+1} &= \mathbf{W}_K \end{aligned} \tag{74}$$

where subscript k denotes the RK stage, α^k are the RK parameters and K is the total number of RK stages. In this work, third-order accurate RK method with the following coefficients was used:

$$\alpha_i = [0.28, 0.61, 1.0] \tag{75}$$

Note that such higher-order RK parameters for optimal damping and smoothing the solutions can be found in [18].

As the RK steps are completed (between the mth and $m+1$st pseudo-iterations) the solution at new pseudo-time level, $\mathbf{W}^{n,m+1}$ is obtained. After each pseudo-iteration level, the convergence check is established by performing relative convergence check between $\mathbf{W}^{n,m+1}$ and $\mathbf{W}^{n,m}$ and finding whether the maximum error in the divergence conditions and the maximum residual among all the state quantities are both smaller than a pre-specified tolerance. Once this condition is satisfied, the pseudo-convergence (i.e. $\partial\mathbf{W}/\partial\tau \to 0$) is achieved and one gets $\mathbf{W}^{n+1,M} \to \mathbf{W}^{n+1}$, the corrected solution at the new time level $n+1$. The numerical experience shows that the pseudo-iterations usually converge within 5–10 iterations each of which includes several RK steps. Note that this semi-implicit procedure is more accurate than the explicit treatments considered in [11, 19] (last two terms of I_τ^* in Equation (73) do not exist in these references).

9. NUMERICAL RESULTS

This section presents numerical test results obtained by the numerical scheme described in this paper. These numerical tests include standard tests for standard benchmark flow tests as well as other interesting tests including heat and mass transfer, radiation, and magnetic effects. The user friendly code presented here was developed such that structured or unstructured meshes filled with triangles can be produced and appropriate initial boundary conditions can be specified on specific windows on the screen by the user prior to the simulations. During the time iterations, desired flow features (color graphs of W and velocity and magnetic field vectors). In addition, the mesh structure can be displayed on the screen anytime. The required GUI libraries for this purpose have originally been developed in C++. All color graphs displayed in this section were obtained by taking the snapshots of the screen, see [12] for details of visualization feature.

For all the test problems presented, the Prandtl number and artificial compressibility parameter were chosen as $Pr = 0.71$ and $\beta^2 = 0.5$, respectively, unless otherwise specified. The number of pseudo-iterations depends on β^2, δ^2, and CFL number used for $\Delta\tau$. The numerical experience shows that although the required number of pseudo-iterations is greater during the initial stage, it reduces to lower values quickly and vanishes as the steady state (in pseudo-time) is reached. In

DOI: 10.1002/fld

addition the residual jacobian matrix increases the pseudo-convergence rate (this behavior will be shown in Figure 5(b).

9.1. Steady/unsteady lid-driven cavity test

In this standard benchmark test problem the temperature, concentration, magnetic, and radiative effects are ignored and both unsteady and steady state features of the code for FC are examined. For this type of convection, the normalization: FC given in Table I, was used, thus leaving the Reynolds number as the only relevant parameter to specify the flow behavior. The solution domain is a square cavity (i.e. $x, y = [0:1]$) with isotropic triangles (an example is shown in Figure 2). In this test the flow is impulsively started by assigning an initial uniform lid velocity. This is done by setting initially all variables to zero except the lid velocity (i.e. $u = 1$ at $y = 1$). The upper lid boundary condition was chosen to be $u = 1$ and $v = 0$ while the other boundaries were assumed to be no-slip walls (i.e. $u = v = 0, \mathrm{d}P/\mathrm{d}n = 0$). In order to check the convergence property of the code, this problem was solved on coarse grid of 21×21 and a fine grid of 81×81 triangles. The steady solutions for the u velocity versus horizontal direction at $x = \frac{1}{2}$ and those for v versus vertical directional $y = \frac{1}{2}$ obtained for two different Reynolds numbers (i.e. $Re = 100$ and 400) are shown in Figure 3. The solutions agree very well with the solutions of Dailey and Pletcher [20], who used clustered grids near boundaries and those of Ghia *et al.* [21], who used very fine grid. In order to examine the spatial and temporal accuracy of the code, the same problem was run by fixing time step at $\Delta t = 0.01$ on a coarse and fine mesh and the time history of u at central point for $Re = 100$ was obtained as shown in Figure 4. As seen, this velocity reaches the same steady state value of $u = -0.205$ at $t = 6.0$ for both the coarse and fine homogeneous isotropic meshes

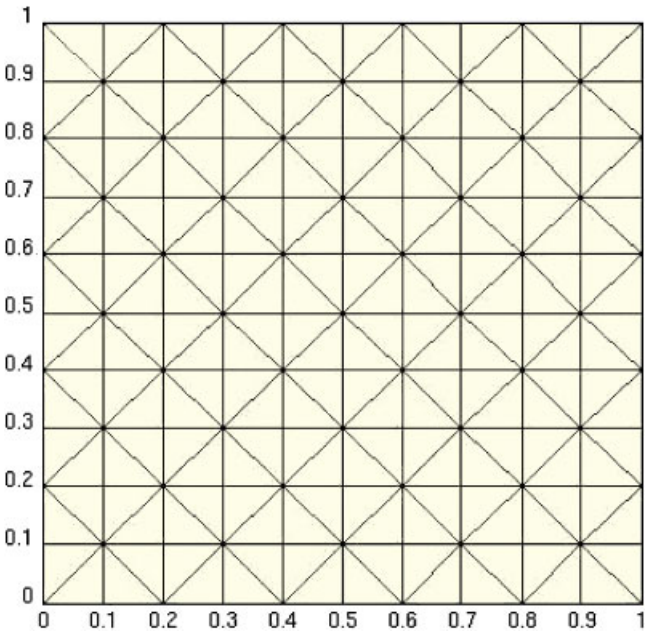

Figure 2. A typical isotropic mesh (11×11) with 121 nodes and 200 triangles.

DOI: 10.1002/fld

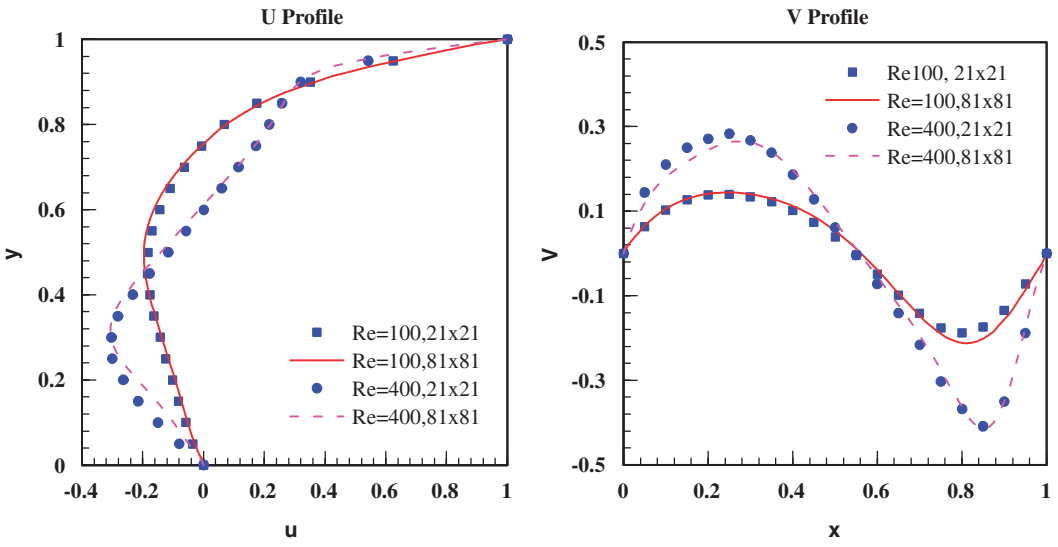

Figure 3. The steady y–u and v–x profiles along centerlines for $Re=100$ and $Re=400$ at 21×21 and 81×81 grids.

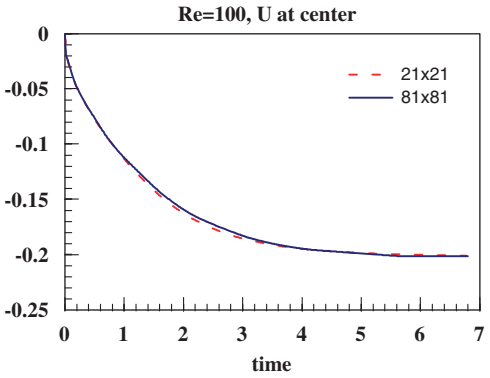

Figure 4. The moving lid test. Time history of u at the center for $Re=100$.

showing that the spatial accuracy of the code is excellent since physically correct solutions are obtained on both coarse and fine meshes. The agreement with the results of Dailey and Pletcher [20] and Pletcher and Chen [22] is again excellent.

In order to examine the effects of time step refinement on temporal accuracy, the same problem was solved with $Re=400$ on the fine grid as done in [20]. The resulting u velocity at the center of the cavity is shown in Figure 5 for three different time steps of 0.1, 0.01 and 0.001, respectively. The local minimum value occurring at $t=6$ is nearly $u_{\min}=-0.20$ and $u=-0.12$ at $t=20$. The same results were given in [20, 22]. This graph shows that the choice of different time steps does

DOI: 10.1002/fld

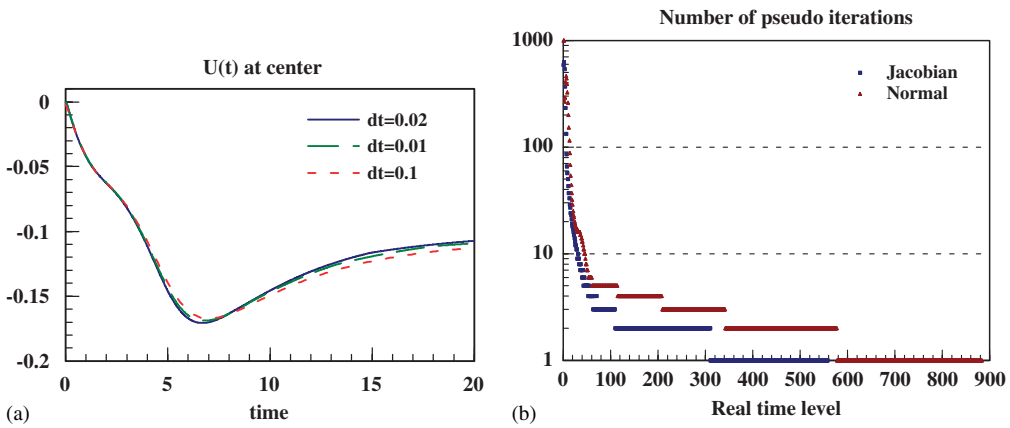

Figure 5. (a) The time step refinement for the lid-driven cavity test and (b) the effect of residual jacobian on the pseudo-iteration levels.

not significantly alter the solutions initially (so temporal accuracy is rather satisfactory) but some numerical errors start to develop at later times whenever larger time steps are used.

9.1.1. Pseudo-iterations. In order to show the effect of the residual jacobian on the pseudo-iterations between real time levels, the steady lid problem was solved on fine grid and the number of pseudo-iterations was counted at each real time level. The resulting graphs with and without residual jacobian are shown in Figure 5(b). As seen, the existence of residual jacobian gives rise to fewer number of pseudo-iterations and provides a quicker overall convergence.

9.2. Unsteady oscillatory lid test

This test problem deals with laminar incompressible flows in a square cavity whose top wall moves with a sinusoidal velocity in time. The lid velocity is given as $u=\cos(t), v=0$ and this was kept as analytical boundary condition on the top boundary and no-slip condition on other walls (i.e. $u=v=0, \mathrm{d}P/\mathrm{d}n=0$). The temporal behavior of the drag force coefficient on the top boundary was approximated numerically by the following second-order three point backward formula:

$$D=\int_0^1 \left(\frac{\partial u}{\partial y}\right) \mathrm{d}x \approx \sum_i \frac{1}{2}\frac{(3u_{i,M}-4u_{i,M-1}+u_{i,M-2})}{\Delta y}\Delta x \tag{76}$$

where subscript i denotes x_i on the top boundary, y_M. As lid velocity is sinusoidal, the drag coefficient shows periodic oscillations as presented in Figure 6 for $Re=400$ for two different grid sizes of 31×31 and 121×121. As seen, although the drag magnitude depends on the grid resolution, the oscillations have the same period regardless of the grid size. This is because, the numerical formula, Equation (76), used for drag calculation depends on both Δx and Δy but not on Δt. As seen from Figure 6, the drag changes within $[-32, +32]$ and the period of the oscillations is nearly 6.2. These values are the same as the results presented in [23], stating that time accurate solutions can be obtained by the code presented here.

DOI: 10.1002/fld

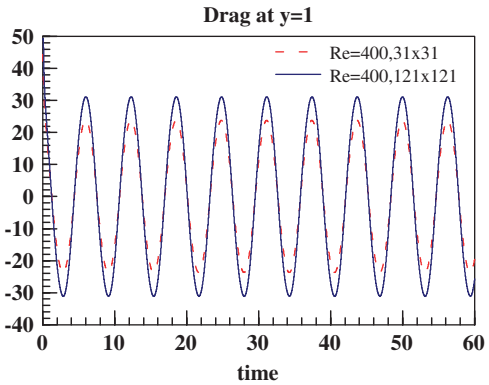

Figure 6. The time history of the drag on the upper lid for sinusoidally changing upper lid velocity for the lid test.

9.3. *Decaying vertices velocity equilibrium*

In this test, temporal and spatial accuracy of the scheme presented here are verified by comparing the numerical solutions with analytically known solution [24] of 2D decaying vortex whose solution is given by:

$$u(x,y,t) = -\cos\pi x \ \sin\pi y e^{-2\pi^2 t/Re}, \quad v(x,y,t) = \sin\pi x \cos\pi y e^{-2\pi^2 t/Re}$$
$$P(x,y,t) = -\tfrac{1}{4}(\cos 2\pi x + \cos 2\pi y) e^{-4\pi^2 t/Re} \tag{77}$$

This test problem was solved in a square mesh of $x, y \in [-\frac{1}{2}, \frac{1}{2}]$ with $Re = 10$ for three different grid sizes of 41×41, 81×81, and 161×161 points. The initial condition was taken as zero velocity and reduced pressure everywhere except boundaries on which analytical solution was used as boundary conditions. The typical color graphs of the numerical solutions of u, v, and P are depicted in Figure 7 for 41×41 mesh. This solution is preserved in time with the exception that the flow behavior remains the same but its magnitude reduces exponentially as given in Equation (77). If the analytical solution is used in the solution domain for initial condition, it was observed that this solution is preserved to an error of machine zero stating that the code is linearity preserving. If zero velocity and pressure are provided as the initial condition, the number of pseudo-iterations is large (near 100) initially since it takes long until the boundary values modify the interior. This number then reduces significantly in the following iterations. In order to examine the effect of artificial compressibility parameter, β^2 on the convergence properties of the scheme, this test problem was run on a 41×41 mesh with different values (i.e. $\beta^2 = 0.2, 1, 10$) and the results are depicted in Figure 8 until $t = 10$. As seen, while the residual convergence at earlier times is closely dependent upon the value of β^2, after nearly $t = 1$ the residual drops to machine zero for all values of β^2. The numerical experience shows that choosing the value of β^2 within the range of [0.2–2] always produces identical results showing that β^2 affects only the number of pseudo-iterations but not the spatial and temporal accuracy.

DOI: 10.1002/fld

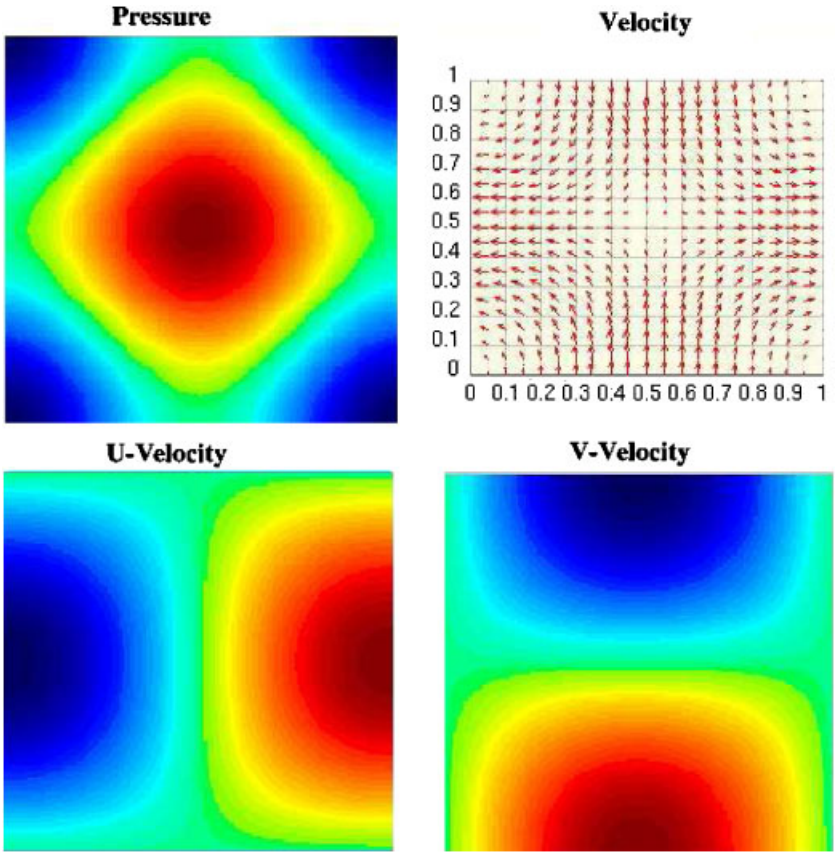

Figure 7. Color graphs of pressure, velocity vectors, and u and v velocity for unsteady decaying vortex test. The solutions were obtained at $t=10$ on a 41×41 mesh using $Re=20$ and $\Delta t=0.01$.

9.4. Flow over a heated electronic component

The fluid flow through a rectangular column produces vortex shedding when the Reynolds number is larger than 50 as demonstrated by Davis and Moore [25], who solved this problem without heat transfer. To understand the effects of vortex shedding on both heat transfer and the flow field around heated electronic components a rectangular region including a heated square was considered. To compare the results of this test with those obtained by Yang and Fu [26], an FC normalization was used with $Re=250$, $Pr=0.71$, and $\Delta t=0.02$, $\beta^2=2.0$. A rectangular region of $x\in[0,18]$, $y\in[0,4]$ was filled with isotropic 7200 triangles and a unit was placed in the central front of the cavity. For implementing boundary conditions, the temperatures were kept at $T=1$ on the nodes of the square object boundary (which is also assumed to be no-slip wall along with upper and lower boundaries). In addition, inlet boundary condition was used on left boundary: $u=1$, $v=0$, and $T=0$ and outgoing boundary condition was used on the right boundary. Note that due to the inherent nature of fluctuation distribution method a boundary becomes an outgoing boundary if no condition is imposed on it. Resulting large structure temperature oscillations around heated

DOI: 10.1002/fld

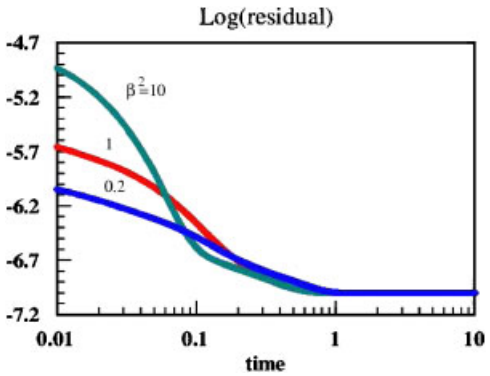

Figure 8. The time history of the log residual as a function of three different artificial compressibility parameters: $\beta^2 = 0.2, 1, 10$.

electronic component at times: $t = 156.2 - 164$ are shown in Figure 9, which includes scanned and reproduced pictures taken from [26]. Comparing the temperature contours of both solutions, it can be seen that the present results and those of [26] have reasonable agreement showing vortex formation behind square and its convection downstream with a reduction in strength. In order to see if this vortex shedding is periodic, the time oscillations of pointwise y velocity on the centerline just behind the square are shown in Figure 10. The unsteady solutions clearly show fully developed periodic oscillations with the same period after $t = 80$, for $Re = 250$. If similar oscillations in v are examined for $Re = 1000$, it can be seen in [26] that the periodic oscillations start after nearly $t = 110$.

9.5. *Boussinesq convection over heated cylinder*

In this test, the temperature effects through BA were examined by using the normalization BC in Table I, hence, the relevant parameters are Prandtl and Rayleigh numbers. This test shows how a heated long cylinder creates convection in cold air under buoyancy effects produced by gravity in the $-y$ direction. To solve this test numerically, a rectangular region including a circle (whose boundary kept at constant temperature) was filled with triangles of 41×41 mesh. Initially all fields were set to zero except the temperature that was taken as $\theta = 1$ on circle boundary. No-slip wall boundary conditions on the circle boundary and free boundary conditions on other boundaries were used. The resulting temperature profiles (with $Pr = 0.72$) obtained at $t = 10$ for different Ra numbers are shown in Figure 11. As seen from these figures, the flow develops and rises around the circle surface absorbing its heat. For small Ra numbers, the flow above circle fills a wide region while it concentrates on the top and thermal boundary layer gets thinner as the Ra number is increased. These results are in excellent agreement with those presented in [27].

9.6. *Thermally driven cavity*

This test is used to simulate heat transfer properties inside cavities and it has a wide range of applications such as building insulation, solar cavities, ventilation, and cooling of electronic devices [28]. For numerical solutions of this test, a square cavity of 41×41 mesh was taken and the Prandtl number was set to 0.71. Initially, all fields were set to zero except the temperatures on the left and

DOI: 10.1002/fld

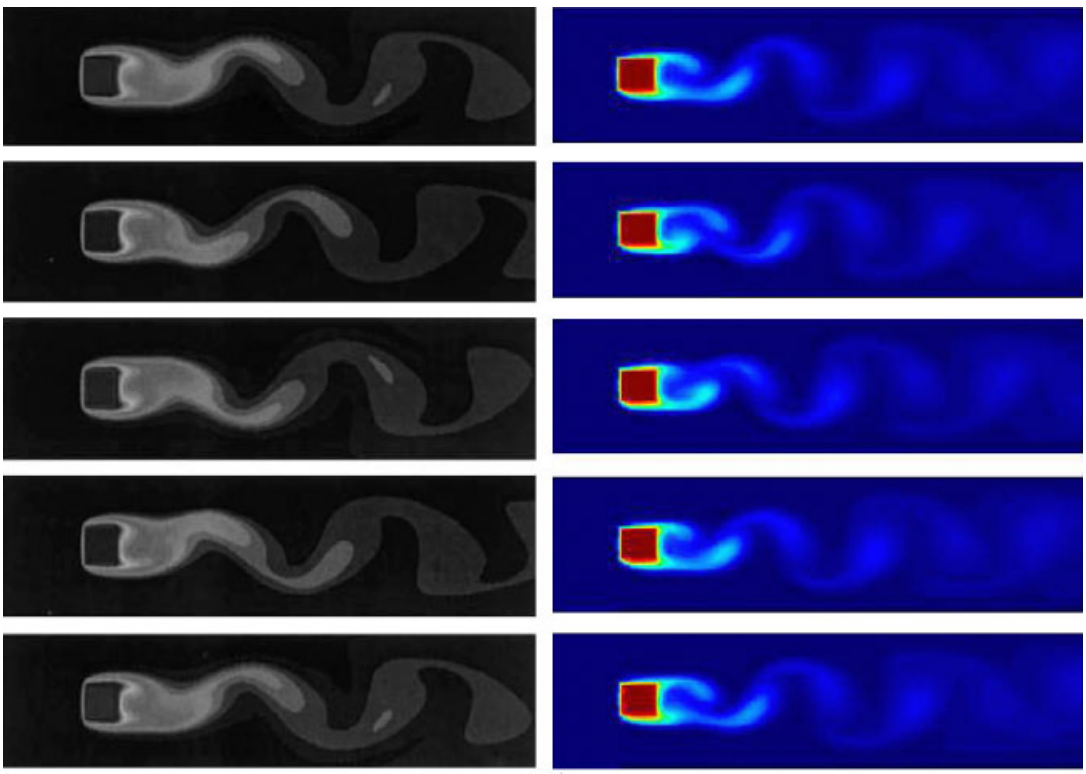

Figure 9. The temperature color graphs for a flow around heated electronic component for $Re=250$ and $Pr=0.71$ at times, $t=156.2, 157.6, 159, 160, 161$ from the top to the bottom. The left figures (a) were scanned and reproduced from [26] and (b) present results for $Re=250$.

right boundaries, which are no-slip walls. The boundary conditions were taken as: $u=v=0$ on the walls, $\theta=1$ on $x=0$, $\theta=0$ on $x=1$, and $\partial\theta/\partial n=0$ on insulating top and bottom walls, $y=0, 1$. It must be noted here that since BC normalization in Table I is used, $\beta^2=1000$ was taken. The resulting temperature and velocity graphs are shown in Figure 12. These results are in excellent agreement with the results of de Vahl Davis [29]. As seen, as the Rayleigh number is increased, the thermal boundary layer on side walls gets thinner and flow separation starts to take place. In order to compare these results numerically with those of other investigators the maximum modulus of the horizontal velocity at vertical centerline, $u_{\max}$, and vertical velocity at horizontal centerline, $v_{\max}$, were obtained on the same 41×41 mesh. The values of these velocities were listed in Table I of Rubio *et al.* [28]. According to this table, several $u_{\max}/v_{\max}$ values for $Ra=10^4$ (obtained by other investigators) are: $\frac{16.064}{19.515}$, $\frac{16.182}{19.509}$, $\frac{16.1630}{19.608}$, $\frac{16.162}{19.614}$ while those for the present work are $\frac{16.136}{19.605}$. For $Ra=10^5$ these values are: $\frac{33.965}{67.562}$, $\frac{35.07}{66.73}$, $\frac{34.81}{68.22}$, $\frac{34.772}{68.329}$ and those for the present work are $\frac{35.355}{69.055}$ and finally for $Ra=10^6$: $\frac{63.951}{209.711}$, $\frac{67.49}{206.32}$, $\frac{65.33}{216.75}$, $\frac{64.082}{214.126}$ and the present work: $\frac{71.841}{226.299}$. From these results one can observe excellent agreement with those reported in the literature for $Ra=10^4$ and 10^5 and close agreement for $Ra=10^6$.

DOI: 10.1002/fld

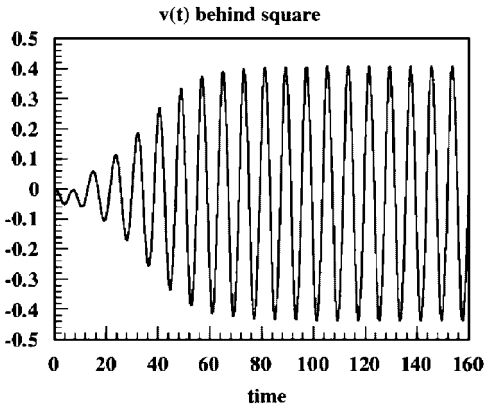

Figure 10. The time oscillations of y-velocity (v) on a point just behind the square whose temperature is kept at $T=1$.

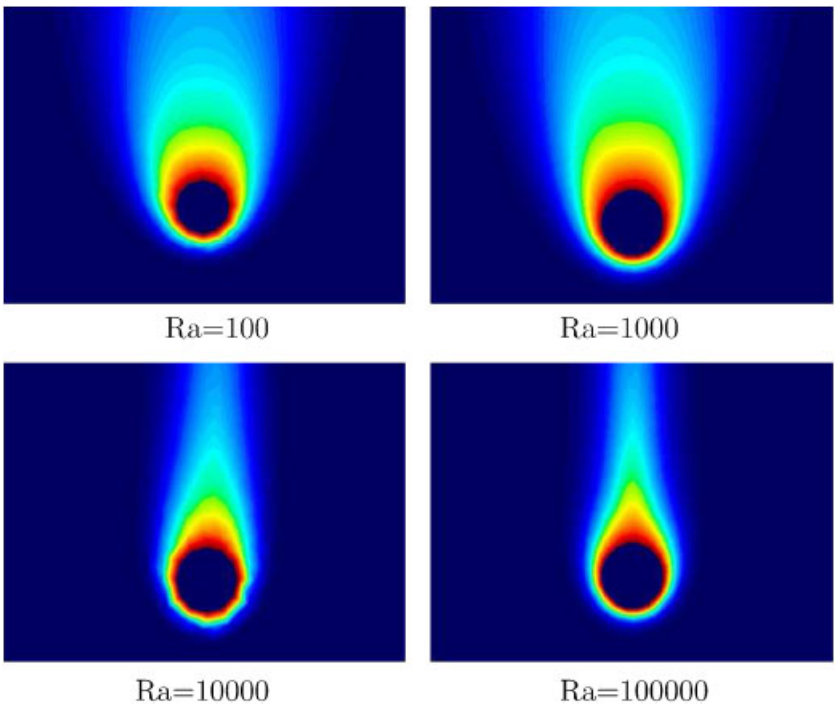

Figure 11. Boussinesq convection around an initially heated circle in a free environment as a function of different Ra numbers, with $Pr=0.72$. Dark regions around circle have higher temperatures.

9.7. Heat and mass transfer test: *salt finger instability*

When heat and mass transfer occur at the same time a complex fluid motion called double-diffusive convection occurs. When temperature and concentration gradients are created in the same

DOI: 10.1002/fld

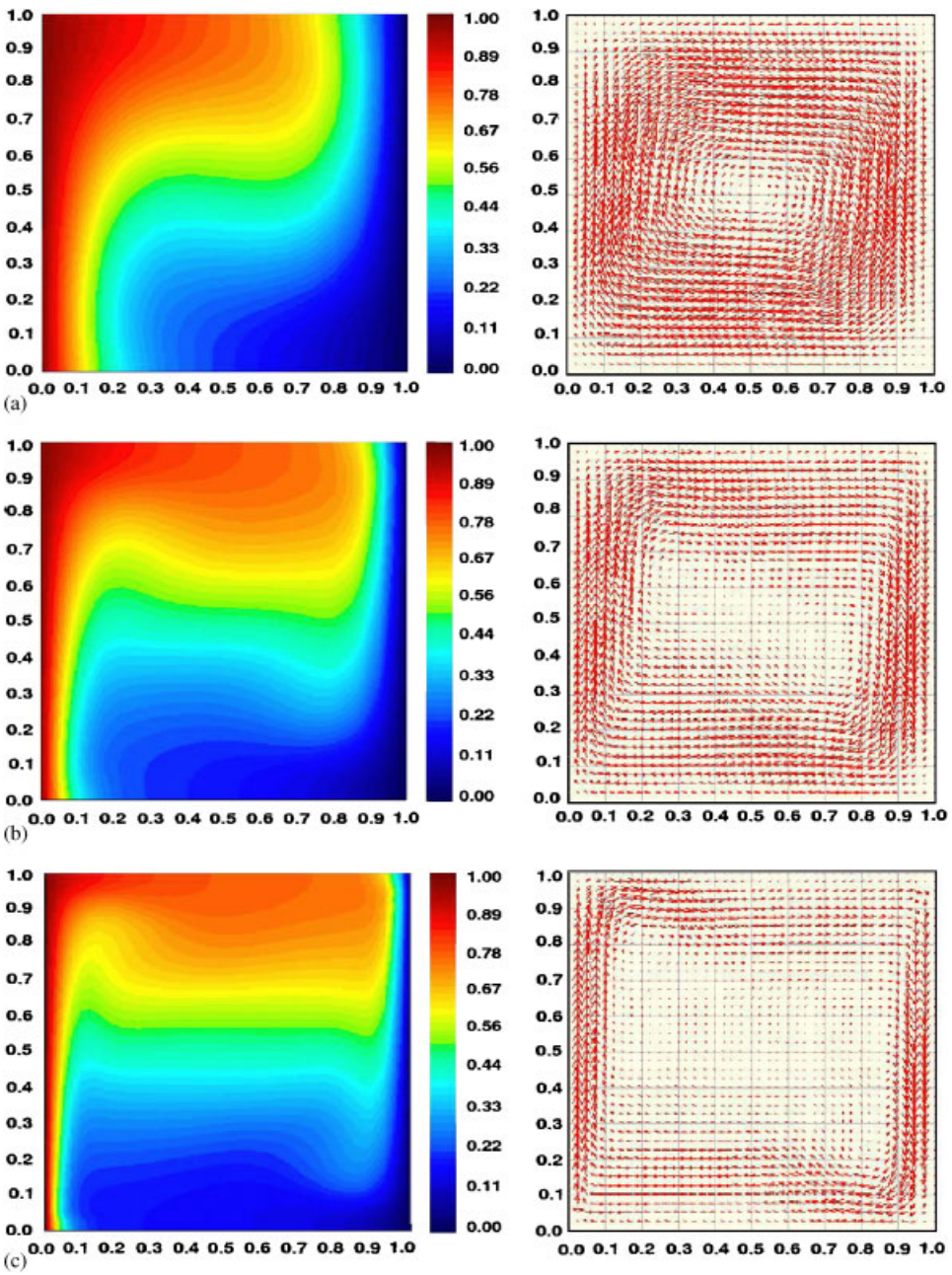

Figure 12. The temperature and velocity graphs obtained from the screen of the code thermally driven cavity test for *Ra* numbers of (a) 10^4; (b) 10^5; and (c) 10^6. All walls are no-slip walls on which $u, v = 0$.

DOI: 10.1002/fld

and opposing directions and the fluid is exposed to magnetic fields, interesting flows (seen in oceanographical, geological, and biological research) can be produced in laboratories. The first test problem was solved in order to investigate the characteristics of hydromagnetic double-diffusive convective flow of a gas mixture in rectangular enclosure with upper and lower walls being insulated [30]. The flow was solved in a rectangular region ($x \in [0, 1]$, $y \in [0, 2]$) whose upper and lower walls are adiabatic and impermeable while the left wall is the source where mixture diffuses to right wall and a constant magnetic field was applied from left to right wall. The initial and boundary conditions can be written as:

$$\begin{aligned} &t = 0 : u = v = 0, \quad \theta = 0, \quad C = 0 \\ &x = 0 : u = v = 0, \quad \theta = 0, \quad C = 0 \\ &x = 1 : u = v = 0, \quad \theta = 1, \quad C = 1 \\ &y = 0, 1 : u = v = 0, \quad \frac{\partial \theta}{\partial y} = 0, \quad \frac{\partial C}{\partial y} = 0 \end{aligned} \tag{78}$$

The parameters $Pr = 1.0$, $Le = 2.0$, $Ra_T = 10^5$, $N = 0.8$ were used along with the DD normalization in Table I. In that case the dimensionless body force for vertical velocity becomes: $-Pr(Ra_T\theta - NC + Ha^2 v)$ where Ha is the Hartmann number representing the magnetic field strength. This problem was solved on a 41×81 rectangular grid until steady state solutions were obtained. The resulting temperature and concentration contours for different Ha numbers are shown in Figure 13 along with those scanned and reproduced from [30]. The agreement of solutions for $Ha = 0$ is excellent but for $Ha = 25$, the concentration contours differ slightly near center. This may be due to the numerical errors introduced when the magnetic term was treated as a source, which was distributed equally to the nodes of triangles.

This test is very important in fuel cell configurations and shows how the salinity and temperature profiles evolve in time after a salty liquid is suddenly exposed into a strong temperature gradient. The onset of finger convection and its dynamics in a stratified fluid layer caused by thermal and salinity motions were investigated experimentally by Chen and Chen [31]. This motion was generated by bringing a warm and solute-rich fluid into contact with side walls, which were kept at constant temperature. If initial salinity and temperature gradients are perpendicular to each other, salt fingers and vortices that last very long times in the domain were observed experimentally in [31]. Ruddick [32] has also made some experiments with heat-salt system to generate property anomalies. They filled a tank with water having salinity gradient and kept its walls warmer or cooler than the room temperature and observed that a regular sequence of salinity layers were produced first at the walls and then grew into the interior of the fluid. The convection layers at the extending noses beyond the fluid are stratified and they create inclined regions (slopes reducing to colder wall) stacked on top of each other. Ruddick [32] realized that these configurations have some relationships to oceanic thermohaline intrusions occurring near oceanic fronts. Since it is difficult to experimentally visualize the behavior of salinity, this original numerical test can be used to investigate how these fingers are formed and why they remain in their specific locations for a long time showing a memory effect. To do that a rectangular cavity of 41×321 mesh with $x \in [0, 1]$ and $y \in [0, 8]$ was considered. BC normalization in Table I was used with $Pr = 0.71$, $Ra = 19600$, $N = 3$, and β^2 was set to 5 and $\Delta t = 0.005$ was taken. Initially, the velocity and temperature fields were set to zero everywhere, except walls and the salinity was set to $S = 1 - y$ so that the salt concentration gets higher toward the bottom. This stationary fluid is suddenly brought

DOI: 10.1002/fld

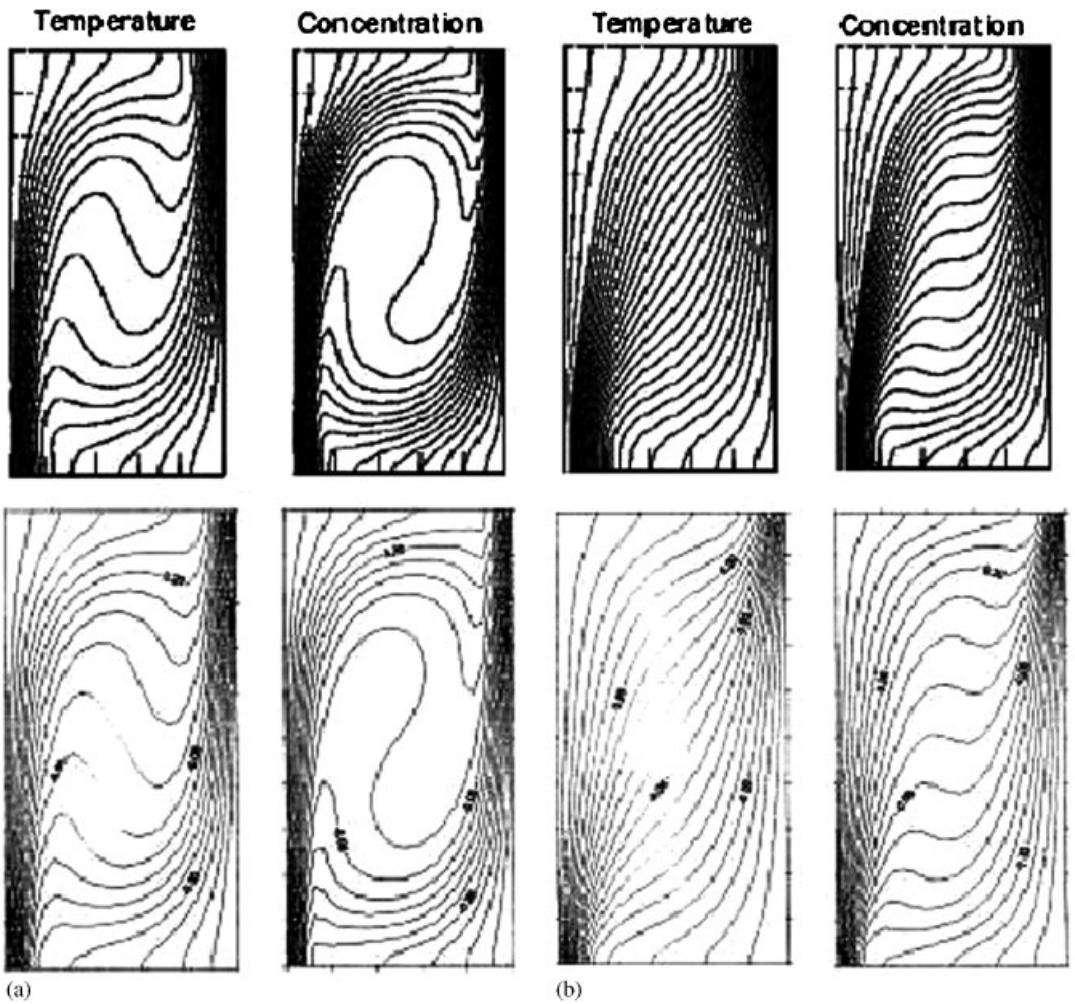

Figure 13. Steady thermal dominated double-diffusive solutions of temperature and concentration reproduced from [30] and current results. The dimensionless parameters are: $Pr=1.0$, $Le=2.0$, $Ra_T=10^5$, $N=0.8$: (a) $Ha=0$ and (b) $Ha=25$.

into contact with hot and cold walls on the right and left walls (kept at $\theta=0$ and 1), respectively. Note that all the walls of cavity were assumed to be no-slip walls with $u=v=0, \mathrm{d}P/\mathrm{d}n=0$ and the salinity values on the lower and upper boundary nodes were kept at $S=0$ and -7, respectively. With these initial and boundary conditions, salt finger instability develops at the bottom near hot wall and rises up due to density and temperature gradients and buoyancy forces. Periodically, new vortices are produced on the top of the other eventually and the whole fluid column is filled with vortices rotating in their fixed locations. This shows that vortices can be stored in fluid once they are successfully developed. This is depicted in Figure 14 as the time evolution of the temperature and salinity at four different times: i.e. $t=40, 100, 150, 180$. As seen the expected instability starts

DOI: 10.1002/fld

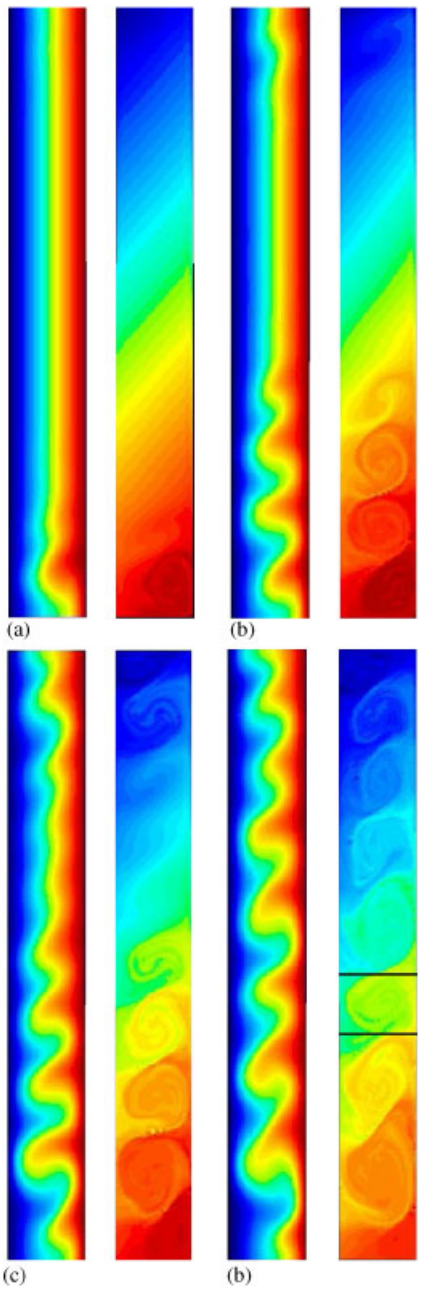

Figure 14. The salt finger instability test. The upper figures show temperature and the lower figures show salinity graphs. The snapshots are taken from the code screen: (a) $t=40$; (b) $t=100$; (c) $t=150$; and (d) $t=180$.

DOI: 10.1002/fld

nearly at $t=40$ and fully develops at $t=180$. The experimental analysis [33] for vertical salinity and horizontal temperature gradients showed that the ratio of dimensionless layer thickness to the wall separation distance was $h/d=0.81\pm0.1$ for Rayleigh numbers ranging from 14 000 to 54 000. This observation was supported by numerical calculations in [34]. In the results presented here (see distance between horizontal lines in Figure 14(d)) it was calculated that $h/d=0.78$ for $Ra=19\,600$. This result is obviously in close agreement with [31, 33, 34]. Similar salt finger development in time can also be seen from the experimental Figure 1 of Ruddick [32] in which the vortices appear near the left wall and propagate almost horizontally toward the other wall.

It must be noted here that after examining the long time behavior of these circulations it was found that the vortices preserve their locations for a long time before they start to decay (until $t=220$). This interesting behavior shows that the fluid has a memory property for a time duration.

9.8. Radiating and magnetized heat and mass transfer

The heat transfer analysis of the high-temperature fields occurring in furnaces, boilers, and gas turbine combustor flows is mainly affected by radiation effects. Some analytical results can be obtained when convection effects can be ignored but the analysis becomes impossible to solve analytically when both radiation and convection are present. The interaction of incompressible, viscous fluid flow with thermal radiation, heat, and mass transfer is also important in hypersonic flows and plasma physics as well as glass production and furnace engineering [35]. The solution of radiation MHD equations requires full radiation transport equations described in Section 3 and is very difficult since random effects should be solved by Monte Carlo techniques. The solutions of full radiative MHD equations are being developed by the author and will be the subject of subsequent publications. The tests considered in this section deal with simple heat and mass transfer effects of an incompressible, viscous, and radiating fluid flow around an impulsively started isothermal hot sheets. For all the tests considered, a constant magnetic field in the x direction was also assumed so that a magnetic source appeared for the v velocity.

Radiation Test.1. In this test one of the simplest problems in which electrically conducting, radiating, viscous, incompressible fluid past an impulsively started infinite vertical plate under the effect of external magnetic field perpendicular to the plate was solved by Mazumdar and Deka [36]. The medium was considered to be optically thick so that the fluid does not absorb its own emitted radiation (non-gray gas near equilibrium). In that case, the radiative heat flux term (source in heat equation) can be taken as: $\partial q/\partial y=\text{const}(T-T_\infty)$, see Cogly *et al.* [6]. Since the temperatures considered are very high, radiative equilibrium condition established in the domain and convective terms can be neglected. In that case, solving the following purely diffusion equations is satisfactory:

$$\frac{\partial v}{\partial t}=\frac{\partial^2 u}{\partial x^2}+\theta-M_{\text{rad}}v \tag{79}$$

$$\frac{\partial \theta}{\partial t}=\frac{1}{Pr}\frac{\partial^2 \theta}{\partial x^2}-\frac{N_{\text{rad}}}{Pr}\theta \tag{80}$$

Notice that the last term in Equation (80) is the dimensionless heat flux term as taken in [6, 36]. To solve this problem with code presented here the convection terms as well as u, C, and $\mathbf{B}$ were set to zero by some parameters, the viscous derivatives in the y direction were set to zero, and obviously Maxwell's equations were not solved. The RC normalization given in Table I was

DOI: 10.1002/fld

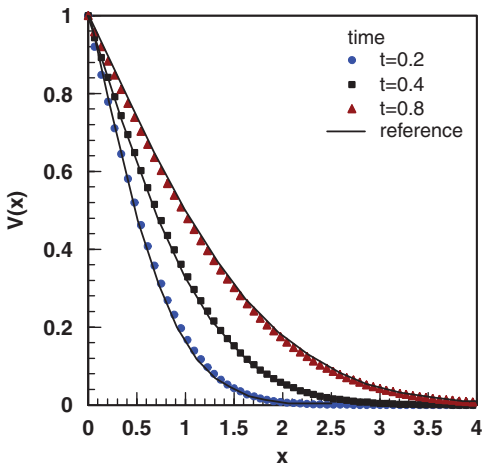

Figure 15. The simple radiating sheet test problem. The graphs show steady state $V(x)$ profiles in the x direction. $Pr=0.71$, $N_{\text{rad}}=0.5$, $M_{\text{rad}}=1.0$, $r=0.0$ were taken.

used along with $M_{\text{rad}}=1$, $N_{\text{rad}}=0.5$, $Pr=0.71$, and $r=0$, $N^*_{\text{heat}}=0$. In that case the source for vertical velocity given by Equation (39) can be taken as simply $S_2=\theta-M_{\text{rad}}v$ where the second term represents the effect of magnetic field. For numerically solving this equation, $\beta^2=20$ was taken and an 81×11 isotropic triangular mesh (with $x:[0:15]$, $y:[0,1]$) was used with $\Delta t=0.01$. Initially, all quantities were set to zero and left and right boundary values were set to: $v=1, \theta=1$ at $x=0$, $v\to 0, \theta\to 0$ as $x\to 0$ while other boundaries were taken as free boundaries as done in [36]. The resulting velocity profiles $y=1$ along x at $t=0.2, 0.4, 0.8$ are given in Figure 15 along with the results given in Figure 15 of [36]. The overlapped graphs obviously show that the time-dependent solutions agree very well. This result shows that the code is able to solve simple radiative non-gray gas flows in optically thick limit.

Radiation Test.2. In this test, steady state free-convection of heat and mass transfer near isothermal sheet affected by buoyancy, concentration, radiation, and transverse magnetic field was solved. The Prandtl number was taken as 3.0 and that the fluid can be considered to be an optically gray medium where the Rosseland approximation is valid. To solve this problem with the code presented, magnetic field was not solved but magnetic effects were introduced as an additional source next to buoyancy terms due to temperature and concentration. In that case, the source for vertical velocity given in Equation (39) can be taken as $S_2=G_r\theta+G_cC-M_{\text{rad}}v$ where G_r and G_c are Grashof numbers for θ. In addition, the radiation source given in Equation (43) was used for temperature. This problem was solved for comparison with the results of Ghaly [4] where they solved the problem by change of variables and using symbolic computation software, Mathematica.

The similar mesh (with $x:[0:15]$, $y:[-1,1]$) and zero initial conditions were used as previous test case but the left and right boundary conditions were taken as: $u=0, v=y, \theta=1, C=1$ at $x=0$ and $\theta\to 0$, $C\to 0$ at $x=15$. According to these conditions it is seen that the sheet moves vertically with a velocity, which is a linear function of y. It must be noted here that there is a fundamental error in this test of Reference [4] since the boundary condition for vertical velocity is not correct as

DOI: 10.1002/fld

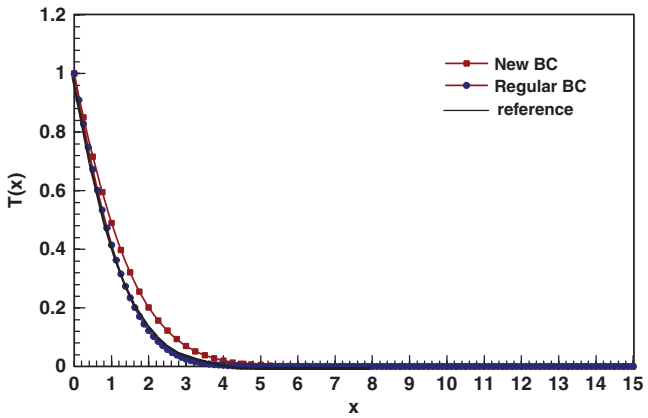

Figure 16. Variation of steady state dimensionless temperature with $Pr=3.0, N_{\text{rad}}=1, M_{\text{rad}}=0.1, r=0.05, Sc=2$.

$x\to\infty$. At large distances, the temperature and concentration are equal to ambient values so that buoyancy terms are zero. In addition, the velocity gradient $\partial v/\partial x$ and diffusion terms are also zero at large distances. In that case the momentum equation reduces to $u\partial v/\partial y=-M_{\text{rad}}v$ showing that vertical velocity changes in the y direction if M_{rad} is non-zero. This result is a contradiction with the constant velocity approximation done in [4] as $x\to\infty$. The correct boundary condition should be free (outgoing) vertical velocity at right boundary. As done in [4], $Pr=3.0, N_{\text{rad}}=1, M_{\text{rad}}=0.1, r=0.05, Sc=2$ were taken and the steady state results were obtained after the convergence was established by the code. Figure 16 gives the overlapping temperature profiles of [4] and numerical results obtained with intentionally used wrong boundary condition (i.e. $v=1$ at $x=15$). The agreement can be seen from the overlapped graphs. Figure 16 also includes the numerical result with free boundary conditions used for vertical velocity. It is seen that the temperature drop is slower with this more consistent boundary condition for velocity.

Radiation Test.3. In this test, the Rosseland approximation was used for optically thin fluid affected by buoyancy forces due to temperature and concentration in the existence of constant magnetic field [35]. The dimensionless vertical velocity and temperature sources were taken as

$$Gr_T\theta+Gr_C C-M_{\text{rad}}v \quad \text{and} \quad \frac{4}{3N_{\text{rad}}}\frac{\partial^2\theta}{\partial y^2}$$

respectively. The initial and boundary conditions were: $u=v=\theta=C=0$ at $t=0$ and $v=1, u=0, \partial\theta/\partial x=\partial C/\partial x=-1$ at $x=0$, $v=0, \theta=0, C=0$ at $y=0$, and $v\to 0, \theta\to 0, C\to 0$ as $x\to\infty$ as done in [35]. The same mesh was used with the following parameters and full convection and viscous terms were retained in the code: $Gr=4, Pr=0.71, N_{\text{rad}}=5, M_{\text{rad}}=1, r=0, Sc=0.6, N=1$. With the time step of $\Delta t=0.01$, this problem was solved in time and the resulting vertical velocity profile at $y=1$ and at $t=8.58$ were presented in Figure 17 along with Figure 3 of [35] as overlapped graph. The velocity is peaked near the wall and eventually reduces to zero away from the plate. The agreement with Reference [35] is again very well proving that the code can accurately solve time-dependent radiative heat transfer problems.

DOI: 10.1002/fld

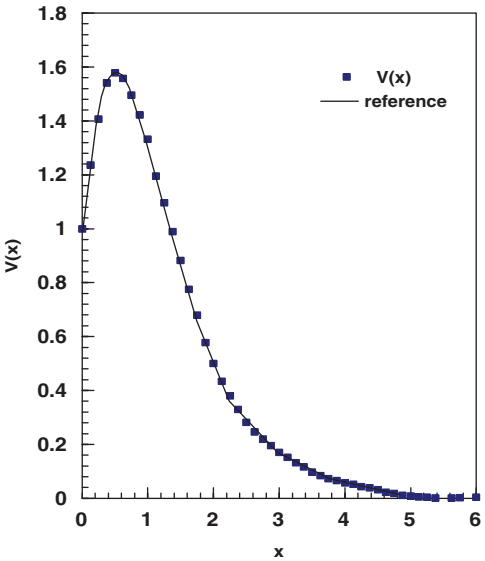

Figure 17. The radiating sheet test problem. The graphs show steady state v profile in the x direction. Used parameters are: $Gr=4$, $Pr=0.71$, $N_{\text{rad}}=5$, $M_{\text{rad}}=1$, $r=0$, $Sc=0.6$, $N=1$.

9.9. Incompressible MHD flow past circular cylinder

This test consists of the flow of a conducting incompressible flow around a perpendicular cylinder under the effects of external magnetic field. This problem was solved as Armero and Simo [37] on a rectangular region of $x\in[-4.5, 15.5]$, $y\in[-4.5, 4.5]$, which is filled with isotropic triangles and which includes a circle of radius 1 with no-slip boundary (i.e. $u=v=0, \mathrm{d}P/\mathrm{d}n=0, \Psi=0$). The left boundary was taken as an inlet boundary with $u=1, v=0$ and all other boundaries were kept untouched during runs (free boundaries). The initial velocity and magnetic field vector were set to zero within the mesh initially. This problem was solved with no magnetic field and aligned (B_x) and perpendicular (B_y) magnetic fields. When magnetic fields are present, all boundaries (including circle surface) were kept at their constant values (i.e. here 1). The non-magnetic solutions with $Re=100$ are unstable since vortices start to shed from circle and create periodic oscillations. The inclusion of magnetic field eliminates this transient response and produces smooth laminar flows. This test was solved with $N=1$, $Re_{\text{m}}=16$, and $Re=100$ in order to compare the results with those of [37]. Note that the Hartmann number (used in [37]) can be obtained from $Ha^2/Re=N/Re_{\text{m}}$ and it takes a value of 2.5 for specified N and Re_{m} numbers, (i.e. the central picture of Figure 12 of Reference [37]).

The resulting time-dependent graphs of u were depicted on Figure 18 with no magnetic field, aligned magnetic field B_x, and perpendicular magnetic field at times: $t_1=10, t_2=80, t_3=120$. As seen from these graphs the flow is made laminar with aligned magnetic field while perpendicular field does a better job and stabilizes the flow totally. Hence, at $Re=100$ and with the magnetic fields included, the flow symmetry is broken but the flow is still laminar. The results with no magnetic field and perpendicular magnetic field correspond and agree well with the top and central pictures in Figure 12 presented in [37]. Another agreement with the results of [37] is that for $Ha=2.5$, the periodic oscillations start nearly after $t=80$.

DOI: 10.1002/fld

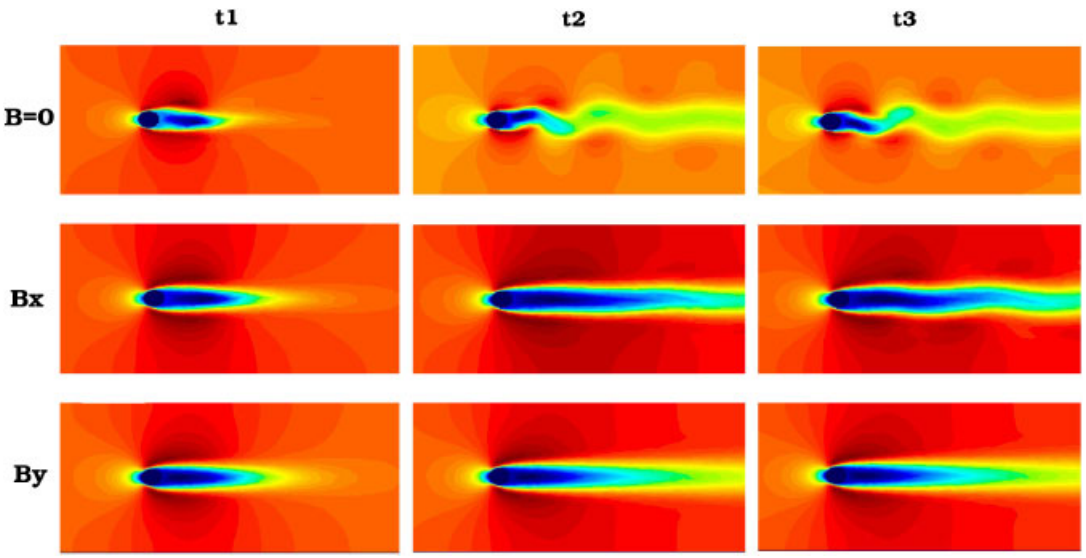

Figure 18. The x-velocity graphs at different times with no magnetic field, with only B_x and with only B_y.

10. CONCLUSION

A numerical code which is able to solve (steady state or transient nonlinear) incompressible MHD equations with mass and heat transfer effects as well as simple radiative effects is presented. The code utilizes a Lax-Wendrof-type MD scheme on structured and unstructured triangles and takes the advantage of dual time stepping for velocity and magnetic field divergence relaxation. The heat and mass transfer effects were considered by Boussinesq approximation. The pseudo-time algorithm includes a simplified jacobian matrix of the residual in order to introduce some implicitness to the multi-stage Runge-Kutta algorithm. With this code, it is possible to choose different normalizations so that the coefficients of viscous terms and sources are handled automatically provided that necessary dimensionless parameters are introduced by user. Several test problems for simple hydrodynamics, heat transfer and diffusion, mass transfer and heat conduction, radiative effects, and finally full MHD flows around cylinder were solved numerically. It is shown by numerical results that the code is reliable and robust and it can be used safely for a variety of 2D problems varying from simple natural flow to radiative charged flows at different concentrations under the effects of external and internal sources. Currently, three-dimensional version of this code is being developed by the author.

ACKNOWLEDGEMENTS

The technical and financial support provided (in 2001 summer) by Prof. Falin Chen from National Taiwan University, Applied Mechanics department was the starting point for this research. It is highly appreciated. Partial support from NATO Collaborative Studies program is also acknowledged. Finally, the computer facility provided by Tubitak, Turkey through the COST project:TBAG-U/166 (105T547) is also acknowledged.

DOI: 10.1002/fld

REFERENCES

1. Ganesan P, Loganathan P. Radiation and mass transfer effects on flow of an incompressible viscous fluid past a moving vertical cylinder. *International Journal of Heat and Mass Transfer* 2002; **45**:4281–4288.
2. Aslan N. Computational investigations of ideal MHD plasmas with discontinuities. *Ph.D. Thesis*, University of Michigan, Nuclear Engineering Department, U.S.A., 1993.
3. Aslan N. MHD-A: a fluctuation splitting wave model for planar magnetohydrodynamics. *Journal of Computational Physics* 1999; **153**:437–466.
4. Ghaly AY. Radiation effects on a certain MHD free-convection flow. *Chaos*, *Solitons and Fractals* 2002; **13**:1843–1850.
5. De Sterck H, Csik A, Vanden Abeele D, Poedts S, Deconinck H. Stationary two-dimensional magntohydrodynamic flows with shocks: characteristic analysis and Grid convergence study. *Journal of Computational Physics* 2001; **166**:28–62.
6. Cogly AC, Vincentine WC, Gilles SE. Differential approximation for radiative transfer in a non-gray gas near equilibrium. *AIAA Journal* 1968; **6**:551–555.
7. Dedner A, Kemm F, Kroner D *et al.* Hyperbolic divergence cleaning for the MHD equations. *Journal of Computational Physics* 2002; **175**:645–673.
8. Choi YH, Merkle CL. The application of preconditioning in viscous flows. *Journal of Computational Physics* 1993; **105**:207–223.
9. Chorin A. A numerical method for solving incompressible viscous flow problems. *Journal of Computational Physics* 1967; **2**(1):12–26.
10. Turkel E. Preconditioned methods for solving the incompressible and low speed compressible equations. *Journal of Computational Physics* 1987; **72**:277–298.
11. Rogers SE, Kwak D. Upwind differencing scheme for the time-accurate incompressible Navier–Stokes equations. *AIAA Journal* 1990; **8**(2):253–262.
12. Aslan N, Onbasioglu E, Balci S, Erdogan A. Parallelization of visual magneto-hydrodynamics code based on fluctuation distribution scheme on triangular grids. *Computers and Fluids* 2007; **36**:961–973.
13. Aslan N. A visual fluctuation splitting scheme for magnetohydrodynamics with a new sonic fix and Euler limit. *Journal of Computational Physics* 2004; **197**:1–27.
14. van der Weide E. Compressible flow simulation on unstructured grids using multi-dimensional upwind schemes. *Ph.D. Thesis*, von Karman Instituut, Sint-Genesius-Rode, Belgium, 1998.
15. Dobez J, Ricchiuto M, Deconinck H. Implicit space-time residual distribution method for unstaeady laminar flow. *Computers and Fluids* 2005; **34**:593–615.
16. Abgrall R. Residual distribution schemes: current status and future trends. *Computers and Fluids* 2006; **35**: 641–669.
17. Zhao Y, Hui Tan H, Zhang B. A high-resolution characteristics-based implicit dual time-stepping VOF Method for free surface flow simulation on unstructured Grids. *Journal of Computational Physics* 2002; **183**:233–273.
18. Gottlieb S, Shu C-W. Total variation diminishing Runge–Kutta schemes. *ICASE Report No. 96-50*, July 1996.
19. Rumsey CL, Sanetrik MD *et al.* Efficiency and accuracy of time-accurate turbulent Navier–Stokes computations. *Computers and Fluids* 1996; **25**(2):217–236.
20. Dailey LD, Pletcher RH. Evaluation of multigrid acceleration for preconditioned time-accurate Navier–Stokes algorithms. *Computers and Fluids* 1996; **25**(8):791–811.
21. Ghia U, Ghia KN, Shin CT. High-Re solutions of incompressible flow using the Navier–Stokes equations and a multigrid method. *Journal of Computational Physics* 1982; **48**:387–411.
22. Pletcher RH, Chen KH. On solving the compressible Navier–Stokes equations. *AIAA Paper*, vol. 48, 1994; No. 94-3368.
23. Granier B, Lerat A, Wu Z-N. An implicit centered scheme for steady and unsteady incompressible two-phase flows. *Computers and Fluids* 1997; **26**(4):373–393.
24. Kim D, Choi H. A second order time-accurate finite volume method for unsteady incompressible flow on hybrid unstructured Grids. *Journal of Computational Physics* 2000; **162**:411–428.
25. Davis RW, Moore EF. A numerical study of vortex shedding from rectangles. *International Journal of Fluid Mechanics* 1982; **116**:475–506.
26. Yang RJ, Fu LM. Thermal and flow analysis of a heated electronic component. *International Journal of Heat and Mass Transfer* 2001; **44**:2261–2275.
27. Sa J-Y, Kwak D. A numerical method for incompressible flow with heat transfer. *NASA Technical Memorandum 110444*, NASA-Ames Research Center, Moffett Field, CA 94035-1000, U.S.A., April 1997.

DOI: 10.1002/fld

28. Rubido O, Bravo E, Claeyssen JR. Thermally driven cavity flow with Neumann condition for the pressure. *Applied Numerical Mathematics* 2002; **40**:327–336.
29. de Vahl Davis G. Natural convection of air in a square cavity: a bench mark numerical solution. *International Journal for Numerical Methods in Fluids* 1983; **3**:249–264.
30. Chamka AJ, Al-Naser H. Hydromagnetic double diffusive convection in a rectangular enclosure with opposing temperature and concentration gradients. *International Journal of Heat and Mass Transfer* 2002; **45**:2465–2483.
31. Chen CF, Chen F. Salt-finger convection generated by lateral heating of a solute gradient. *Journal of Fluid Mechanics* 1997; **352**:161–176.
32. Ruddick B. Laboratory studies of interleaving. *Progress in Oceanography* 2003; **56**:529–547.
33. Chen CF, Briggs DG, Wirtz RA. Stability of thermal convection in a salinity gradient due to lateral heating. *International Journal of Heat and Mass Transfer* 1971; **14**:57–65.
34. Wirtz RA, Briggs DG, Chen CF. Physical and numerical experiments on layered convection in a density stratified fluid. *Geophysical Fluid Dynamics* 1972; **3**:265–288.
35. Ramachandra Prasad V, Bhaskar Reddy N, Muthucumaraswamy R. Transient radiative hydromagnetic free convection flow past an impulsively started vertical plate with uniform heat and mass flux. *Theoretical and Applied Mechanics* 2006; **33**(1):31–63.
36. Mazumdar MK, Deka RK. MHD flow past and impulsively started infinite vertical plate in presence of thermal radiation. *Romanian Journal of Physics* 2007; **52**:565–573.
37. Armero F, Simo JC. Long-term dissipativity of time stepping algorithms for and abstract evolution equation with applications to the incompressible MHD and Navier–Stokes equations. *Computer Methods in Applied Mechanics and Engineering* 1996; **131**:41–90.

DOI: 10.1002/fld